Università degli Studi di Padova

Dipartimento di Ingegneria Industriale
Corso di Laurea Magistrale in Ingegneria Aerospaziale

Tesi di Laurea Magistrale

CFD Simulation of a Transonic Fan: Mesh sensitivity study, mapping and 3D validation

Laureando:
Marco Zennaro

Relatore:
Prof. Ernesto Benini

Correlatore:
Ing. Andrea Magrini

Anno accademico 2019 / 2020

Alla mia famiglia,
a Chiara
per il loro sostegno durante questo percorso

Nomenclature

$UHBPR$	Ultra High Bypass Ratio
B, BPR	Bypass Ratio
TPR	Total Pressure Ratio
TTR	Total Pressure Ratio
$p\ [Pa]$	Static Pressure
$p^0\ [Pa]$	Total Pressure
$T\ [K]$	Static Temperature
$T^0\ [K]$	Total Temperature
η_{ad}	Adiabatic Efficiency
$\dot{m}\ [kg/s]$	Mass flow rate
$\dot{m}_c$	Corrected mass flow rate
$N\ [RPM]$	Rotational speed
N_c	Corrected Rotational speed
M_∞	Freestream Mach number
SDT	Source Diagnostic Test
LDV	Laser Data Acquisition
RAN	Rotor Alone Nacelle
MF	Mesh Fine
MM	Mesh Medium
MC	Mesh Coarse
MEC	Mesh Extra Coarse
GCI	Grid Convergence Index
$R4$	Rotor Blade
OGV	Outlet Guide Vane
$L.E.$	Leading Edge
$T.E.$	Trailing Edge
SST	Shear Stress Tensor
RNG	Re-Normalisation Group

Contents

Sommario

Lo sviluppo tecnologico e la richiesta di prestazioni sempre migliori per i sistemi propulsivi sono frutto di una progettazione sempre più dettagliata. Il raggiungimento di risultati così accurati è possibile grazie all'utilizzo dell'approccio computazionale alla risoluzione delle equazioni del moto. Nel campo della propulsione per velivoli ad uso civile, a differenza dei velivoli militari, tra i requisiti più stringenti troviamo, oltre a quelli di natura ingegneristica, quelli di natura economica ed ambientale. Le diverse aziende produttrici di motori aeronautici hanno indirizzato le loro risorse alla progettazione e produzione di motori ad alta efficienza propulsiva. Questo passaggio, inizialmente ottenuto mediante sistemi turbofan ad alto rapporto di bypass, ha permesso un risparmio in termini di consumo di combustibile e, di conseguenza, vantaggi di natura economica e ambientale. Un altro aspetto fondamentale, è stata la riduzione del rumore prodotto da questi apparati e, proprio grazie agli studi ed agli esperimenti condotti da questa branca di ricerca, è stato possibile sviluppare la seguente tesi.
Nel processo di investigazione sulle sorgenti principali del rumore prodotto da un fan ad alto rapporto di bypass, la NASA ha ricreato un modello in scala di un motore rappresentativo dello stato dell'arte di questa categoria di sistemi propulsivi. Oltre ai risultati riguardanti il rumore prodotto da questi sistemi, sono state condotte misure di natura aerodinamica sulle performance del fan. Lo scopo di questa tesi è stato quello di ricreare, mediante un modello CFD, i risultati ottenuti sperimentalmente in galleria del vento. Prima di giungere alla simulazione del modello completo, è stato eseguito uno studio di sensitività sulla mesh del canale interno: così facendo è stato possibile ridurre considerevolmente il numero di elementi utilizzati e risparmiare in termini di tempo di simulazione e di risorse hardware necessarie. Per la validazione del modello sono stati utilizzati i valori sperimentali in termini di: prestazioni fornite (mappa del fan) e velocità misurate. Un ulteriore termine di paragone è stato offerto dai risultati di una simulazione NASA dello stesso apparato sperimentale. Per ottenere il modello finale sono stati dapprima creati dei modelli in Single passage. Una volta validato il modello del singolo canale contenente un unico elemento palare è stato possibile aggiungere l'influenza del campo esterno e completare lo stadio con lo statore.

- I -

Introduction

This M.Sc. thesis has the main purpose of addressing a complex problem through the use of a commercial software developed by ANSYS: Cfx. This software was born as a dedicated tool for the study of turbomachinery fluid dynamics and allows the transition from an analytical design with formulas and empirical laws to a high-fidelity simulation of real physical laws governed by the differential Navier-Stokes equations. This design strategy, if done properly, will save time, find more efficient solutions and reduce prototyping costs. The time needed to solve a problem depending on the type of problem, the geometry and consequently, on the mesh chosen for its discretization. In the design process, it is therefore essential to be able to approach a problem as efficiently as possible.
Before describing in detail the problem and the strategies used, a few basic concepts and the quantities used will be recalled.

1.1 Civil Propulsion State of Art

From the first flight in the history of humanity to the world-famous supersonic civil transport aircraft, the Concorde, humanity has always tried to overcome its limits, innovating and experimenting, with the fundamental objective of flying longer and more efficiently. After the Second World War, part of the knowledge and technologies developed were dedicated to civil aviation, the turbojet engine is an outstanding example. This type of engine allows to reach higher speeds than those achieved with propeller propulsion. A turbojet engine, also called gas turbine engine, is nothing more than a gas generator with intake and a nozzle. The gas generator consists of a compressor, a combustion chamber and a turbine designed to drive the compressor. Figure 1.1 shows a diagram of a typical gas turbine engine, air is guided by the intake to the axial compressor that increasing, by the action of multiple stages, its pressure. The next step is the mixing of the air with the fuel

and burning them in the combustion chamber. The hot gases pass through the turbine and are finally accelerated by the nozzle to obtain the thrust.

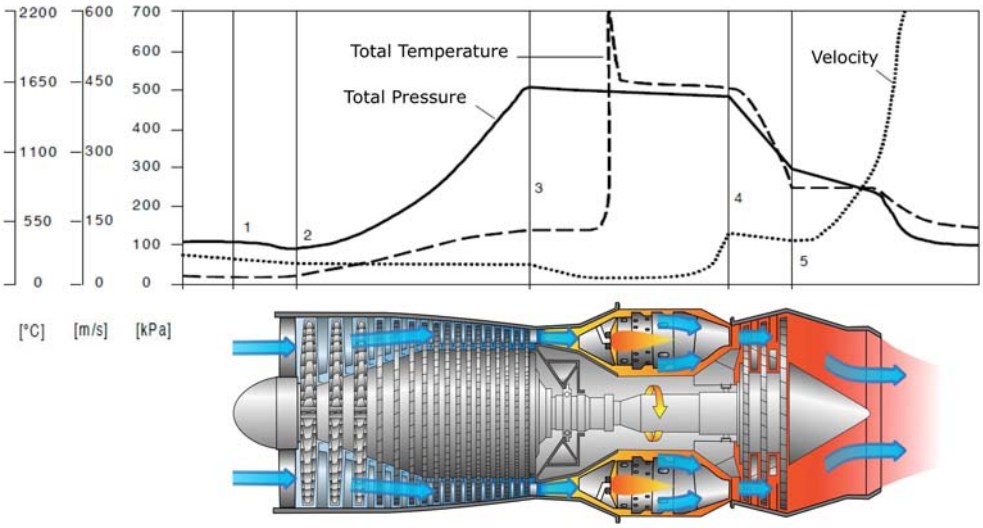

Figure 1.1: *Diagram of properties variation inside Turbojet engine (cit. Hill - Peterson [9])*

With the aim of reducing specific consumption, or the TSFC (Thrust Fuel Specific Consumption), this type of engine has been replaced by Turbofan: a turbojet with the addition of a Fan (low compression ratio compressor). These engine categories are in turn divided into two sub-groups: separate streams generally adopted for civil propulsion, and mixed streams mainly adopted in military aircrafts. The Fan generally has a much larger diameter compared to the diameter of the first stage of the compressor, this allows it to process a higher mass flow rate and therefore, maintaining the same thrust produced with a decrease in the TSFC. The turbine will have to maintain both the compressor and the fan, so it is generally divided into high-pressure turbine (HP turbine) and low-pressure turbine (LP turbine). As it is subjected to greater expansion, the fluid coming out of the combustion chamber will reach the inlet of the nozzle with a total temperature lower than in the case of a simple turbojet.
The thrust obtained from the core engine will be lower than a simple turbojet but the advantages can be observed by the large flow rate processed by the Fan. In Figure 1.2 are summarize the performance of an unmixed turbofan with $\text{Mach}_\infty = 0.85$, this value is representative of cruise flight condition for civil aircraft.

These curves were obtained considering air as the ideal gas model and considering only one-dimensional gas dynamics. Analyzing these graphs it is possible to observe how an increase in the bypass ratio B causes an increase in propulsive efficiency in contrast to the thermal efficiency, which instead decreases. The overall efficiency curves show that there is an improvement in performance for the range of pressures generally adopted. It is also observed that there is a limit value that the bypass ratio does not make sense to

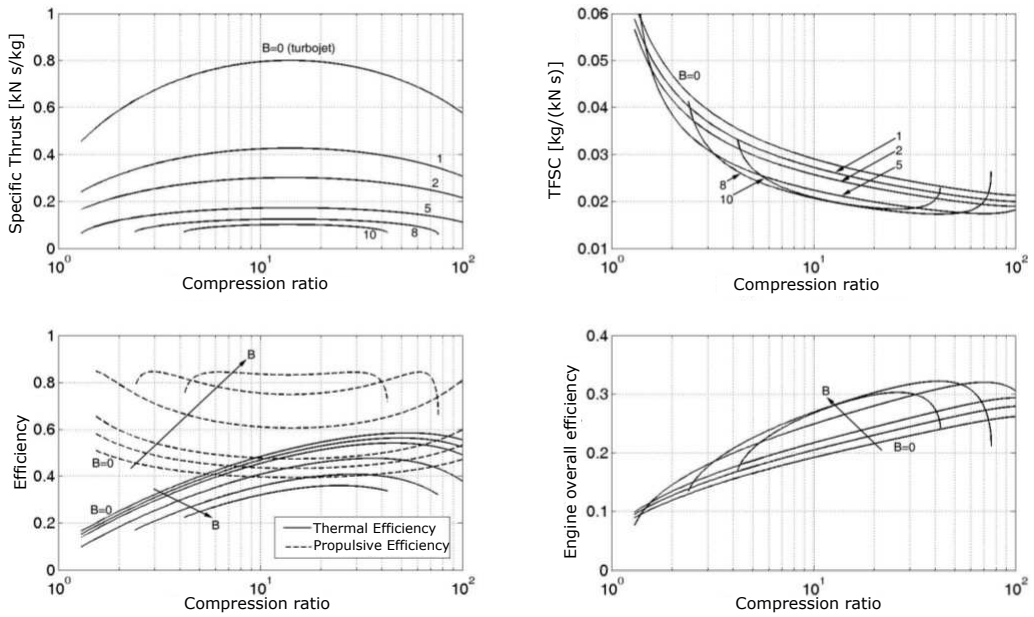

Figure 1.2: *Turbofan engine characteristics curves with $Mach_\infty = 0.85$ (cit. Benini [8])*

exceed, B = 10. Using realistic models it is observed that the maximum value of B can exceed B = 15. In this thesis the focus will be only on the fan, so the following paragraphs summarize the main equations and thermodynamic transformations that occur in this type of turbomachinery.

1.2 Axial Compressors

An axial compressor is a turbomachinery with the purpose of increasing the fluid pressure up to the value required by the combustion chamber. In addition to axial machines, there are also centrifugal machines capable of achieving compression and would also offer much higher single-stage compression ratios than an axial machine (4-6 compared to 1.1-1.3) but these are characterized by a 5-6% lower efficiency than axial machines. The combination of all the stages of an axial compressor allows to produce a compression ratio that can vary from 8 to 40: this great achievable value and the lower production costs compared to a centrifugal machine make axial machines the most used. An improvement adopted in the compressors is the use of variable stators developed by GE (General Electric), in fact the possibility to modify the pitch angle allows an adjustment of the mass flow rate and an operating range of variable pressure ratio thus having a greater control on the stall margin. The variable stators are divided into three categories according to their

positioning, starting from the inlet and continuing in an axial direction: IGV (Inlet Guide Vanes), VDV (Variable Stator Vanes) and OGV (Outlet Guide Vanes).

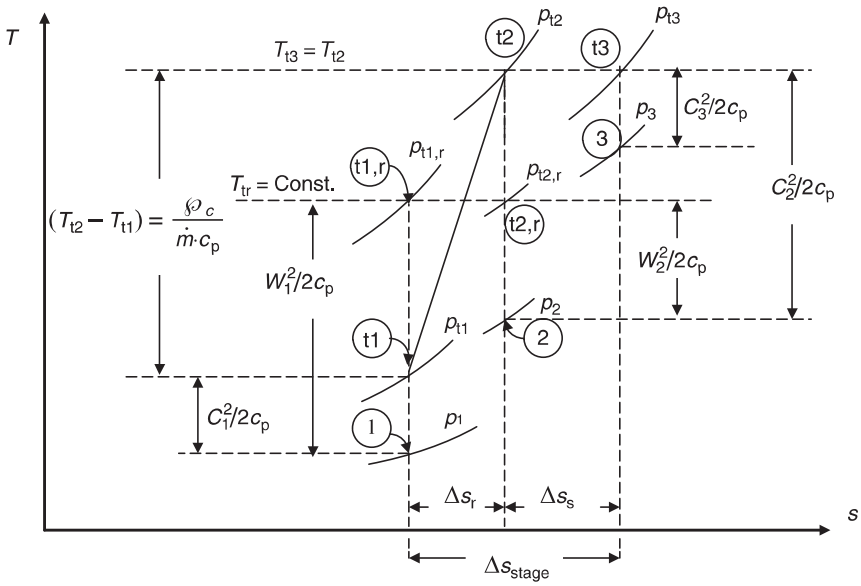

Figure 1.3: *Absolute and relative state of gas in a compressor stage (cit. Farokhi [10])*

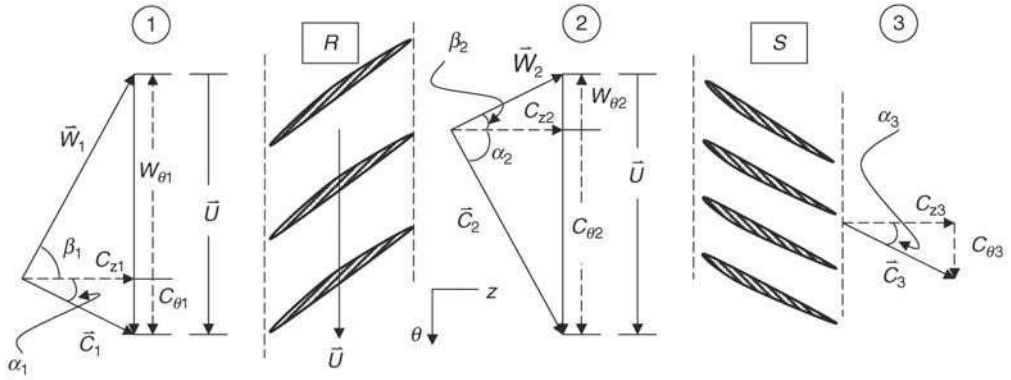

Figure 1.4: *Absolute and relative flow angles in a compressor stage (cit. Farokhi [10])*

Figures 1.3 and 1.4 show respectively the complete transformation within a compressor stage and a diagram of the relative and absolute speeds taken at the mid radius of the blade.

1.2.1 Efficiency

Efficiency is a measure that describes the quality of the transformation performed by the turbomachinery. Isentropic efficiency can be defined considering total or static states as follows:

$$\eta_{iso} = \frac{L_{iso}}{L} = \frac{\Delta h_{iso}}{\Delta h}$$

$$\eta_{iso,t-t} = \frac{L_{iso}}{L} = \frac{\Delta h^0_{iso}}{\Delta h^0}$$

the second formulation is more suitable for compressible fluid machines operating at high speeds. Using the ideal gas model at constant specific heat, and the laws of isentropic transformations, it is possible to relate the enthalpy state to temperature and pressure.

$$\eta_{iso,t-t} = \frac{\pi_c^{\left(\frac{k-1}{k}\right)} - 1}{\frac{T_2^0}{T_1^0} - 1}$$

where 1 indicates the upstream conditions and 2 indicates the downstream state. The definition of efficiency just described, however, does not consider losses of a thermofluid-dynamic nature and it is a function of the pressure ratio. All these limits are exceeded by introducing the polytropic efficiency. The polytropic efficiency in fact would be much more suitable to judge the quality of an aerodynamic design and it is defined as the adiabatic efficiency of an adiabatic thermodynamic process whose pressure ratio is infinitesimal.

$$\eta_{pol} = \frac{dh_{is}}{dh} = \frac{dp/\rho}{c_p dT} = \frac{k-1}{k} \frac{\ln\left(\frac{p_2^0}{p_1^0}\right)}{\ln\left(\frac{T_2^0}{T_1^0}\right)}$$

1.2.2 Transonic Fans

Technological progress in metal alloys has made it possible to create high-strength, low-mass titanium blades, thus making it possible to extend the concept of turbofan by greatly increasing the size of the fan. Since these machines have a high rotation speed, different motion conditions are created at various blade heights: from a relative subsonic flow at the hub to a relative supersonic flow at the tip. In addition to the possibility to increase the size, modern fans have increased the compression ratio of the single stage up to 1.6. This improvement therefore makes it possible to use fewer stages to achieve the desired overall compression ratio. The savings are therefore both economic and in terms of weight.

In a transonic cascade, the increase of the static pressure is mainly due to the crossing of oblique or almost normal shock waves, so the current deviation is very limited. Unlike a completely subsonic stage, in a transonic stage the profiles subject to supersonic flow are morphologically different: they have a reduced thickness and pointed at the leading edge. A subsonic profile, if invested by a relative supersonic current, develops a curved

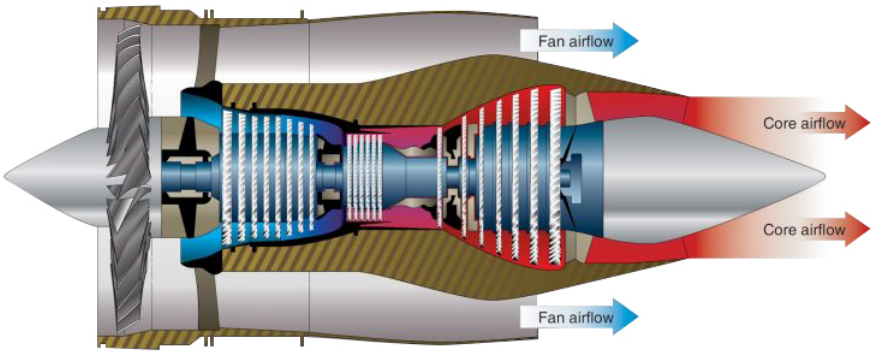

Figure 1.5: *Diagram of high-bypass Turbofan Engine (cit. Types of Gas Turbine Engines. - Newfoxy)*

wavefront and detached from the profile. This condition has to be avoided by generating oblique shocks attached to the profile. The accurate geometrical shape of transonic profiles may not be enough: if a stage is subject to a large pressure ratio and the angle between relative current and tangent to the chamber line is small, the detached impact may occur. This condition is representative of a rotor with a mass flow rate close to stall, so it is a condition to be avoided as downstream pressure waves can rise again influencing the inlet conditions and consequently the turbomachinery.

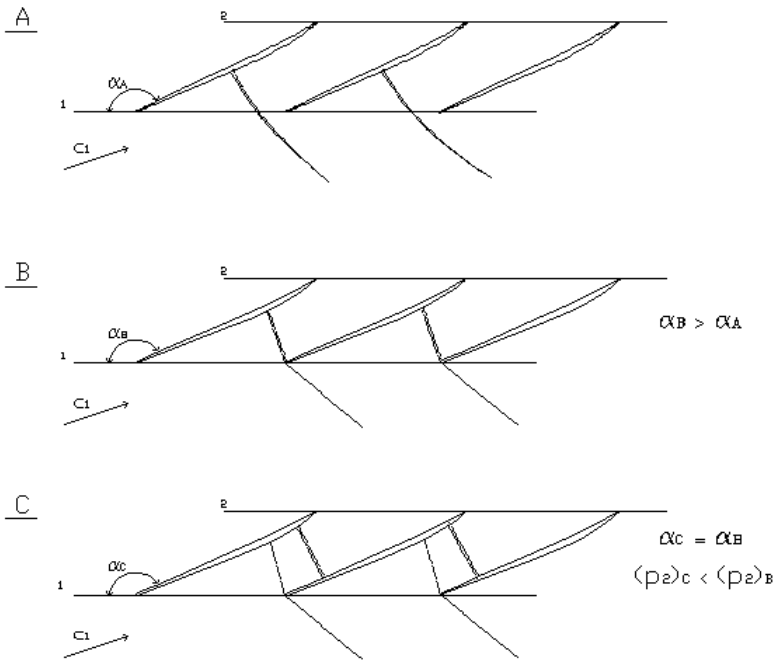

Figure 1.6: *Transonic Cascade - flow configuration (cit. Benini [8])*

Figure 1.6 (A) represents the case just mentioned. Figure 1.6 (B) is obtained when the mass flow rate at the inlet is that of chocking, in this case the depression waves coming

from downstream can at most reach the position of the shock wave without affecting the operating conditions of the compressor. Finally case 1.6 (C) is obtained starting from case B and further reducing the downstream pressure.

1.3 Compressor Maps

The compressor maps are graphs summarizing the operating characteristics of the turbomachinery. The graphs are parametric for the correct rotation speed of the machine and show the compression ratio and the Efficiency as a function of the correct mass flow rate processed. The correct quantities, or their functions, are used so that the graphs are independent of the upstream fluid conditions.

$$\dot{m}_c = \dot{m}\frac{\sqrt{\theta}}{\delta}$$

$$N_c = (RPM_c) = \frac{N}{\sqrt{\theta}}$$

where $\theta = \frac{T_1^0}{T_{ref}^0}$ is the temperature correction to standard day and N is the revolution per minute and $\delta = \frac{p_1^0}{p_{ref}^0}$ is the pressure correction.

Frequently the iso-efficiency curves are shown directly in the pressure ratio graph, so it is possible to have all the characteristic quantities in a single plot.
The compressor map is obtained experimentally by connecting the turbomachinery to a wind tunnel. By keeping the upstream conditions fixed, the discharge pressure and the rotation speed of the machine are modified, thus obtaining all the curves shown in the figure.

The points on the compressor map define the following zones:

- Surge line: it represents the boundary between the condition of minimum flow rate that can be processed at that speed of rotation and the stall. The second condition obviously represents an unstable operation. The current assumes a positive incidence angle and it is possible to observe the phenomenon of boundary layer detachment with the consequent restriction of the duct.

- Chocking: this condition is represented by the vertical asymptote that each speedline presents, it is the maximum that can be processed by the machine. The angle of the

current is deviated and different from the design conditions, this produces a decay of the compressor performance.

- Operating line: as it can be observed this line tries to interpose itself between the two conditions by reaching as much as possible the maximum efficiency.

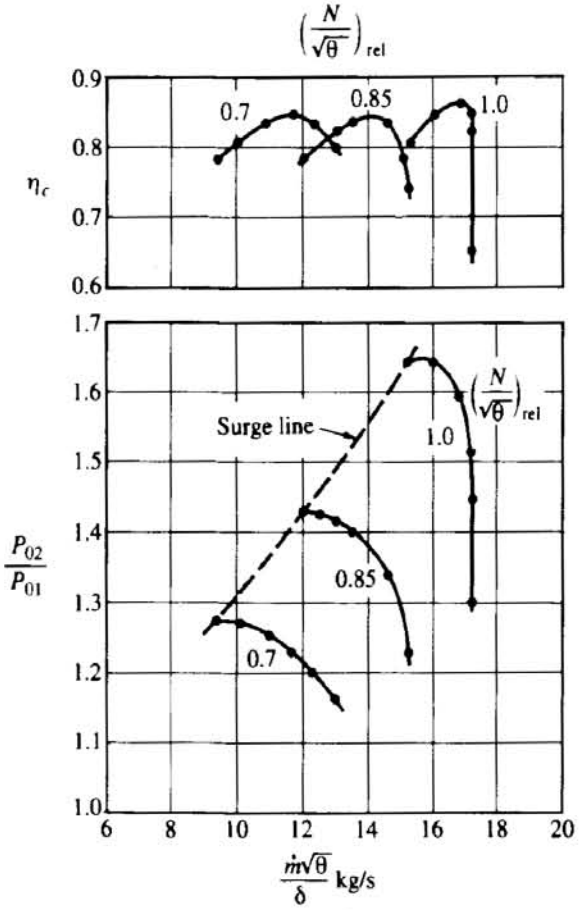

Figure 1.7: *Compressor map (cit. Hill - Peterson [9])*

1.4 Subsonic Inlet

The Intake is the component that conveys air from outside to inside the engine. Depending on the flight condition there will be subsonic Intake and supersonic Intake. Hugoniot's equation describes the behavior of the fluid through this component as well as providing the geometric shape for subsonic inlet:

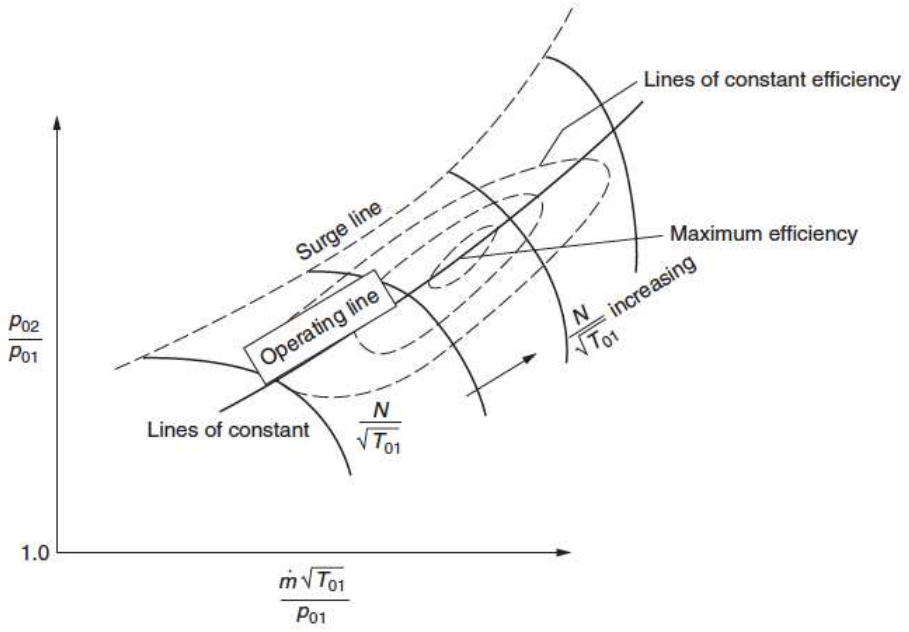

Figure 1.8: *Compressor map with Iso-efficiency curves (cit. Hill - Peterson [9])*

$$\frac{dc}{c} = -\frac{dA}{A}\frac{1}{(1-M_\infty^2)}$$

Figure 1.9 shows two possible flow conditions and their thermodynamic transformation for a subsonic Intake. Using the continuity equation and assuming that the upstream flow of the intake is isentropic, the upstream capture area can be related to the intake area. The suctioned mass flow rate for an aircraft proceeding with a certain M_∞ at an altitude with p_a and T_a is defined by the following equation

$$\dot{m}_a = \frac{p_a}{\sqrt{\frac{RT_a}{k}}} M_\infty A_a$$

the mass flow rate through intake area is defined as:

$$\dot{m}_1 = \rho_1 A_1 c_1$$

in conclusion, depending on the flight Mach number, the following cases may occur:

- $A_a/A_1 < 1$, this condition of flow diffusion before intake is called Overspeeding condition and has an additional component of resistance to motion, so it is a condition to be avoided as much as possible.
- $A_a/A_1 > 1$ this configuration arises when the engine is hit by a particularly slow subsonic current: generally this condition occurs in take-off conditions. If this condition occurs, the diffusion effect of the intake is zero.

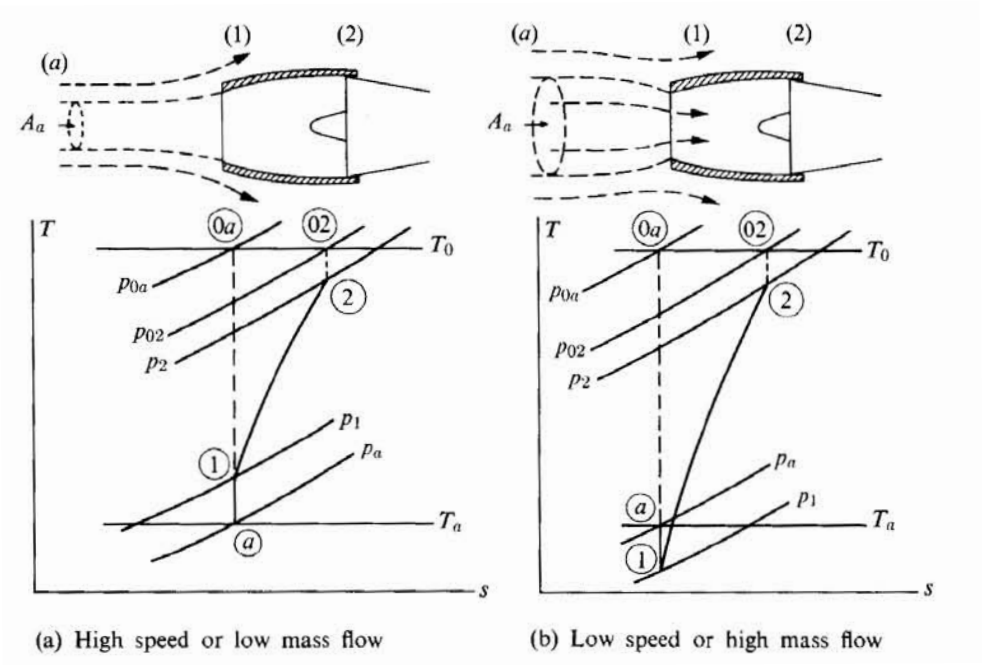

Figure 1.9: *Subsonic Inlet configuration (cit. Hill - Peterson [9])*

1.5 Purposes and Scope of work

Technological progress is allowing more powerful and performing resources to be made available, but the role of the engineer in the control of operations and problem management remains crucial. Specifically, this thesis focused on the relationship between the reliability of the model created and its discretization, all related to a Fluid dynamics problem. The main aim was the creation of a CFD model with as few elements as possible that was able to best represent the physics that concerned it. The final result was achieved by successive steps: before creating the complete model of the system, a Single Passage analysis was carried out. A sensitivity study was performed on this Mesh with the relative calculation of the errors incurred as a result of the process of reducing the element number. Once the convergence of the simulation was reached, the results were compared with the experimental measurements. The model in Single Passage was validated and it was possible to pass to the implementation of the complete model consisting of Rotor, Stator, Nacelle and external domain by performing a Full-Annulus analysis. By changing the boundary conditions three speedlines of the fan (60,87.5,100% Nc) in Take-off condition were mapped. The comparison with the experimental results made it possible to modify the mesh in the areas of interest, thus allowing an improvement of the calculated solution.

- II -

Test case and Model setup

In this chapter the test case developed by NASA at the Glenn Research Center in the 9x15 Low Speed Wind Tunnel will be presented. The experiment was born with the aim of identifying the sources of noise that arise in a turbofan engine with a high bypass ratio. The fan rotor was designed by General Electric Aircraft Engines and called R4. The objectives of the thesis and the guidelines for the creation of the various models and the setting of the simulations will also be described.

2.1 Fan Module: R4

Most of the available experimental results come from a NASA-developed test case called SDT (Source Diagnostics Test) conducted in the 9 by 15 Foot Low-Speed Wind Tunnel. The SDT test was born mainly to study the noise generated by a fan with a high bypass ratio, in order to identify the sources of this phenomenon and consequently act locally to reduce it. The fan selected for the study is called R4 and it is a 1/5-scale model that represents the state of the art of the high bypass ratio turbofan. The R4 was mapped to different speedline, also were used, depending on the measurement to be made, two different Inlet: the bellmouth Inlet and a flight-type Nacelle. Different configurations for the stators were also analyzed, measuring the influence on the performance of the stage and the fan. Table 2.1 summarizes the parameters of the fan.
Table 2.2 summarizes the Fan performance (RAN and Baseline OGV) for three speedlines: Approach (61.7), Cutback (87.5), Take-off (100%), corrected fan speed, respectively 7809, 11075 and 12657 RPMc.

Fan performance at the three operating point reported have been obtained by testing the fan at sea level with fixed nozzle area by changing the rotation speed.
The envelope of the points managed with this procedure create the fixed nozzle operating line. The constant Nc lines were obtained by modifying the experimental apparatus and

N° of Fan Blades	22
Fan Tip Diameter	0.56
Hub/Tip Ratio	0.30
Corrected RPM	12657

Table 2.1: *Fan design parameters*

RPMc	$\dot{m}_c$ $[kg/s]$		TPR		TTR		Adiab. Eff.	
	RAN	Fan/OGV	RAN	Fan/OGV	RAN	Fan/OGV	RAN	Fan/OGV
7809	26.7800	26.4444	1.158	1.159	1.048	1.049	0.8909	0.888
11075	38.0654	38.0609	1.359	1.360	1.102	1.102	0.9010	0.9020
12657	43.8397	44.0801	1.511	1.509	1.138	1.136	0.9092	0.9136

Table 2.2: *Fan design performance*

installing a VFEN (Variable Fan Exit Nozzle) thus modifying the outlet area but keeping the rotation speed constant, so it was possible to vary the flow rate processed by the fan and consequently draw the speed line.

As shown in the Figure 2.1,2.2 and 2.3 the operating line would seem to be close to the Surge line, but this is due only to the fact that during the experiment NASA kept away from this condition so the lower flow rate points are to be understood as the last experimental measurements and not as stall flow rates of the respective speedline.
The three points of the operating line marked with solid symbols are very important and will often be recalled in the followig analyses, for example for calculating the performance along the blade span. Once the fan map with CFD analysis has been performed, the three points mentioned above, which are characterized by a mass flow rate, a TPR and aTTR, will be searched within the available points of the three speed lines of the map in order to validate the CFD model.

2.2 Mesh sensitivity study

In each CFD simulation the time needed for convergence or to complete the required number of iterations is an important parameter that must be taken into account. CFX is a finite volume software so the greater the discretization the greater the time needed for the simulation. Depending on the type of analysis and on the type of resources available it is necessary to make a trade-off between the discretization and the time available for the simulation.
Usually the simulation of a turbomachinery, in this case of a fan, starts with the analysis

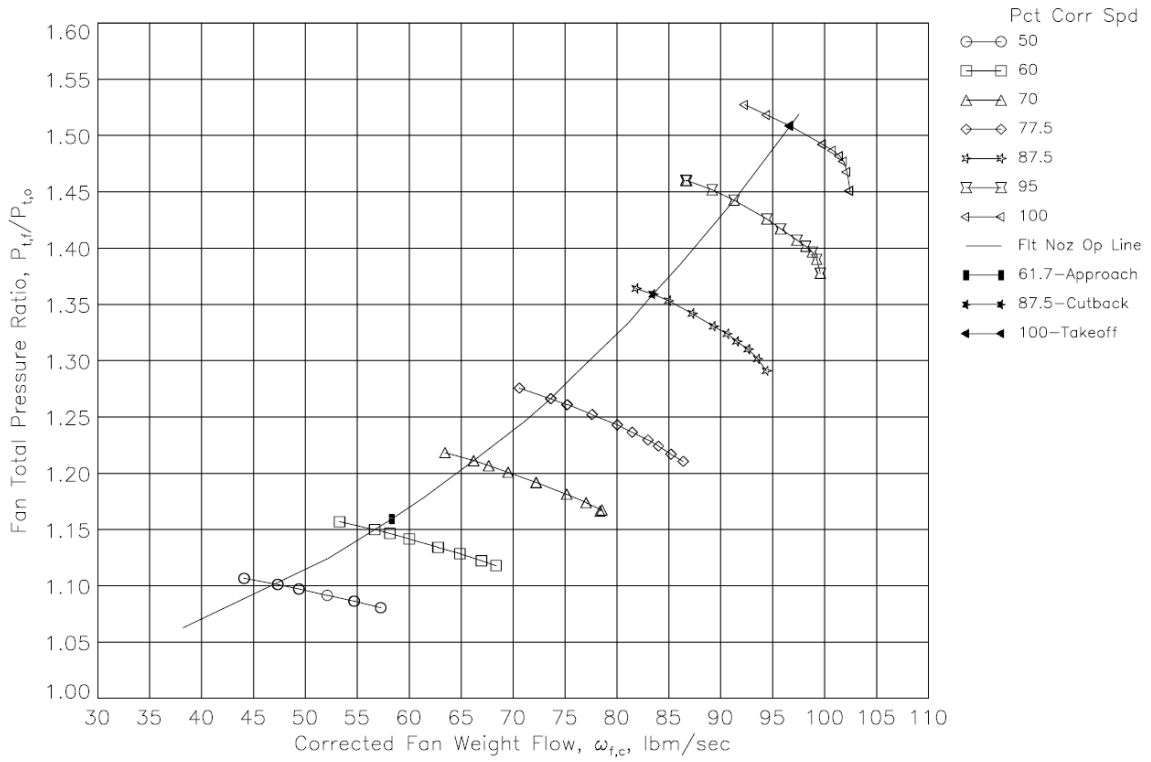

Figure 2.1: *Total pressure ratio of the FAN with Low Noise OGV [3].*

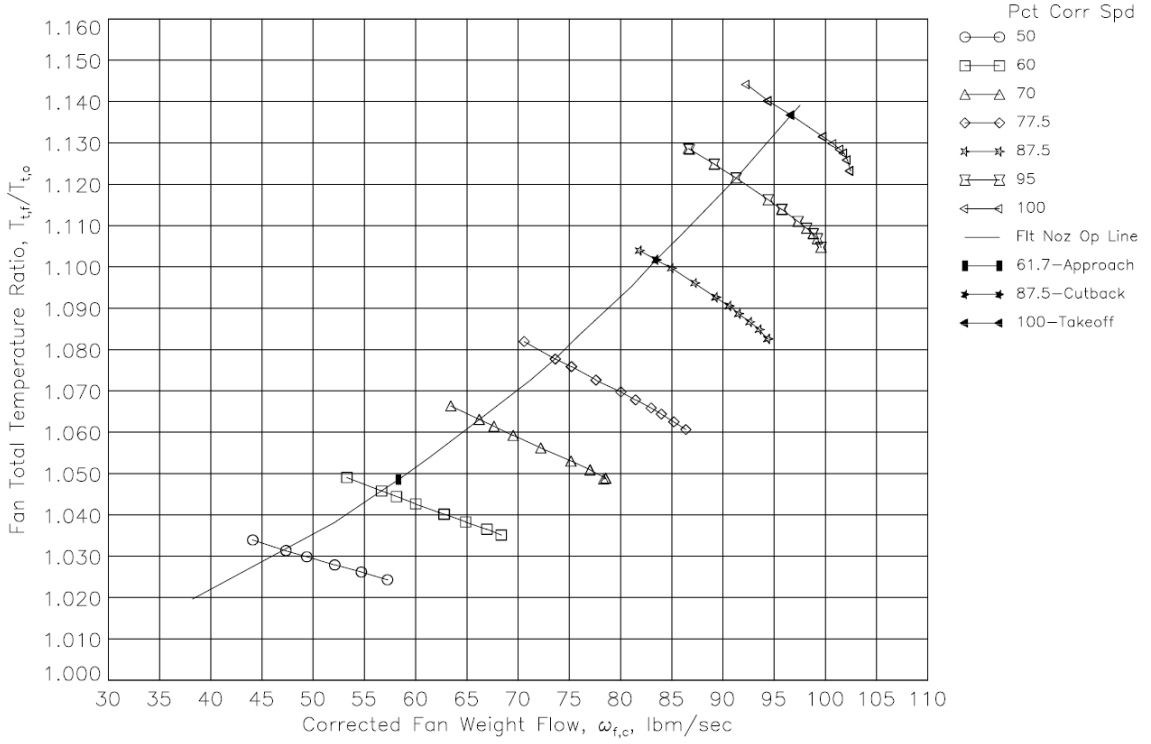

Figure 2.2: *Total temperature ratio of the FAN with Low Noise OGV [3].*

of a fraction of its volume: this type of analysis is called Single passage. For simulations of this type, the volume is discretized with a very dense mesh to better describe the prop-

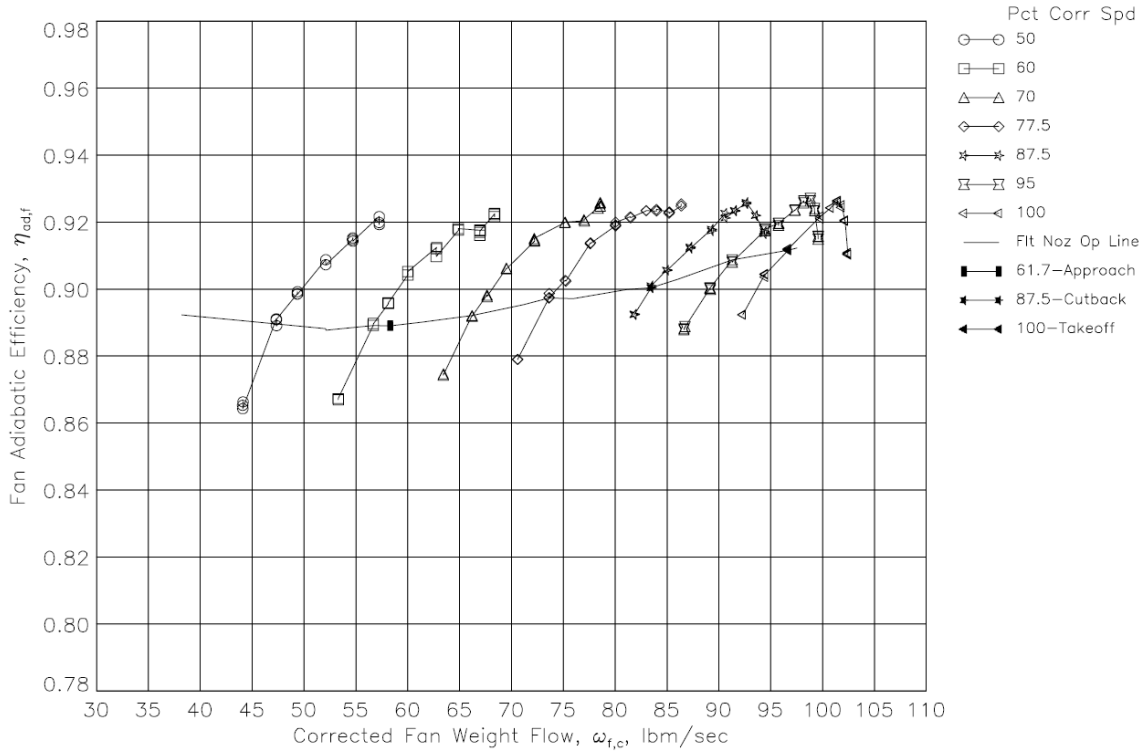

Figure 2.3: *Adiabatic Efficiency of the FAN with Low Noise OGV [3].*

erties of the fluid. Once the validation for the Single passage model has been done, the next step is to perform a Full-annulus analysis by simulating the system in its entirety. In order to reduce as much as possible the number of elements, and consequently the nodes of the mesh, without giving up a realistic description of the physical phenomenon, a mesh sensitivity study is carried out.

2.2.1 Single passage - Inner flow channel

The creation of the different meshes was based on the guidelines provided by GCI (Grid Convergence Method), a recognized method for the estimation of error and uncertainty due to discretization in CFD analysis [5]. This method has been tested on several hundred CFD cases and it is therefore considered valid for this type of calculation. In addition to the calculation of different quantities based on a variable considered representative of the flow (Total Pressure, Total Temperature, Adiabatic Efficiency, etc.) some advice is given on how the refinement between one mesh and another one can be implemented. Generally, in case of structured meshes, the ratio between the number of elements of a mesh and the homologous refined mesh should be 1:3. Consider for example a cube discretized

with 9 elements on each side, in total there will be 729 elements (9x9x9); a refined mesh should have 729x3=2187 elements, this means that each side of the cube will have to be discretized with 12.98 elements, therefore to the nearest integer number.

In recent versions of CFX it is no longer possible to create structured meshes in the blade region. It is in fact allowed using different models of the ATM Topology optimized topology, which automatically recognizes Leading Edge and Trailing Edge of the element to be discretized (Rotor, Stator, Splitter, etc..). With this mesh method it is possible to create block-structured meshes. It is possible also to thicken or thin the areas of interest depending on the pattern chosen. In addition, customized topologies can be recreated to discretize the element according to the user's preferences, this option has been adopted in some meshes created.

Finally, for the creation of the different meshes was considered the CFD study developed by NASA, which describes and reports the methodologies adopted and the mesh size [4]. Treating different channel geometries it was not possible to recreate the mesh used but the information reported was very important and provided a guideline on the procedure to be used as well as providing an order of magnitude on the number of elements to be adopted for a study of this kind. The CFD study also presented several results in terms of Fan performance (processed mass, Total pressure ratio, Total Temperature ratio), results that will be used as a comparison for model validation.
Table 2.3 summarizes all the parameters and information of the various meshes created divided by the regions of the flow field. Figure 2.4 instead presents a view of the discretized fluid channel.

In the two new meshes the discretization of the most sensitive areas has been refined. The wake has been modelled with much more elements than the previous cases by subtracting them from the area between L.E. and T.E. of the blade.
The table 2.4 summarizes the parameters adopted for the two Extra coarse meshes and anticipates a substantial difference between the two: the choice of the turbulence model. This aspect will be discussed in the next section.

2.2.2 Single passage - Inner and Outer flow channel

All the meshes described up to this point concern only the internal fluid dynamics. For obtaining better results and closer to the experimental measurement, it was necessary to

File name	Mesh Fine	Mesh Medium	Mesh Coarse	Mesh NASA
Topology	Single Round Round Symmetric	LECircle High TECircle High	Single Round Round Symmetric	H−O−H
n° Nodes(All domains)	3886874	2059310	1547450	2192858
n° Elements (All domains)	3779666	1988376	1489560	2111890
n° Elements spanwise	162	120	100	85
n° Elements θ	39	36	29	49
n° Elements Axial dir.	89	85	79	217
Node Count				
Passage	2839714	1455240	1057700	1272566
Inlet	827200	397010	341250	492900
Outlet	219960	207060	148500	427392
Element Count				
Passage	2779029	1415112	1027040	1229575
Inlet	794937	378432	323640	473340
Outlet	205700	194832	138880	408975

Table 2.3: *Mesh Data*

File name	MEC_SST	MEC_RNG
Topology	L.E. low T.E. High	L.E. low T.E. High
n° Nodes (All domains)	1590727	1402371
n° Elements (All domains)	1531296	1346100
n° Elements spanwise	76	76
n° Elements θ	46	46
n° Elements Axial dir.	86	86
Node Count		
Passage	937964	749608
Inlet	308555	308555
Outlet	344208	344208
Element Count		
Passage	907896	722700
Inlet	294400	294400
Outlet	329000	329000

Table 2.4: *Mesh Extra Coarse*

enlarge the domain to include the nacelle and a reasonable portion of undisturbed air. Differently from the previous case, with this model configuration it is possible to detect the suction effects produced by the intake. In this type of analysis the stators were also considered (standard short-chord stator), so it was possible to remove the swirl velocity component, otherwise it would have been necessary to change the geometry of the nacelle at the nozzle to be able to refer to the operating conditions described in [3].

As reported in [3], where different types of stators are analyzed, there are no substantial differences in fan and stage performance, it is therefore possible to refer to the same maps shown in the previous paragraph without any loss of generality (Figure 2.1,2.2 and 2.3). The stators used have been discretized with turbogrid in a similar process as for the rotor,

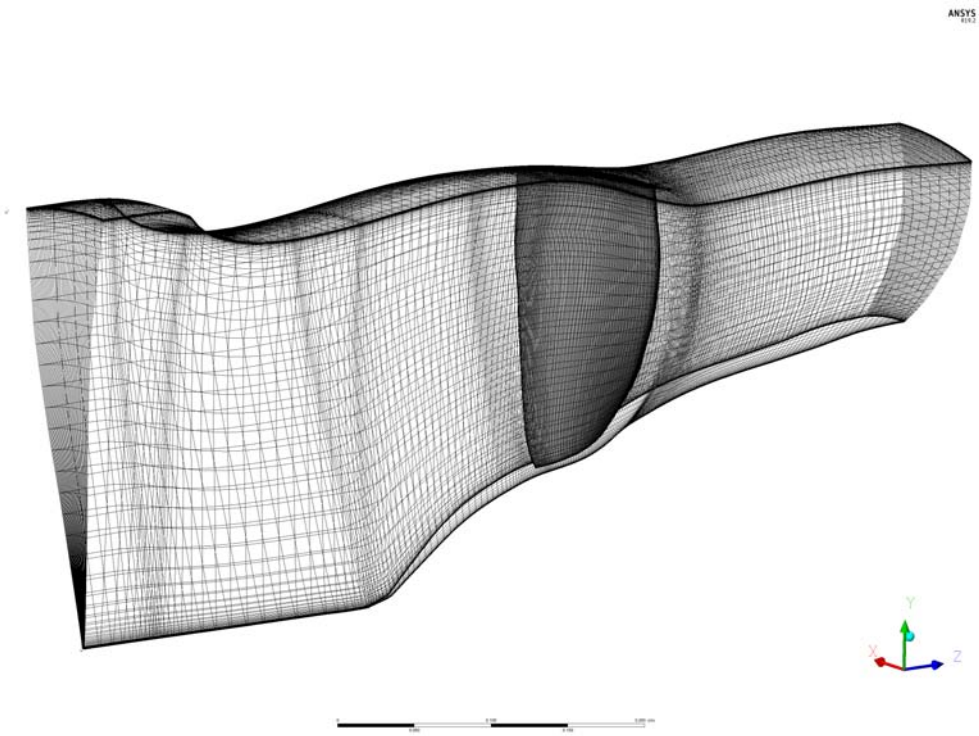

Figure 2.4: *3D view of Inlet-Rotor-Outlet grid.*

however, considerably reducing the number of elements due to the different nature of the component. With this type of fluid channel only the speedline 12657 rpmc was analyzed. The internal channel has been discretized starting from the fine mesh modifying it to add the stator. The Outlet has been extended until the end of the nacelle to recreate the real fan nozzle. Starting from the fine mesh it is possible to minimize the discretization error and highlight any differences from the previous case where the nacelle and the external field of the engine were not simulated. Figure 2.5 and 2.6 show a view of the discretized fluid channel for this type of simulation.

Once the analysis for the 100% speedline was performed using the fine mesh for the internal channel, a further analysis was performed by replacing the fine mesh with the extra coarse mesh from the previous sensitivity study, obviously adapting it slightly to accommodate the stator. The results obtained from this analysis were finally used as the initial solution for the Full-annuls analysis by multiplying them to cover the entire volume of turbofan.

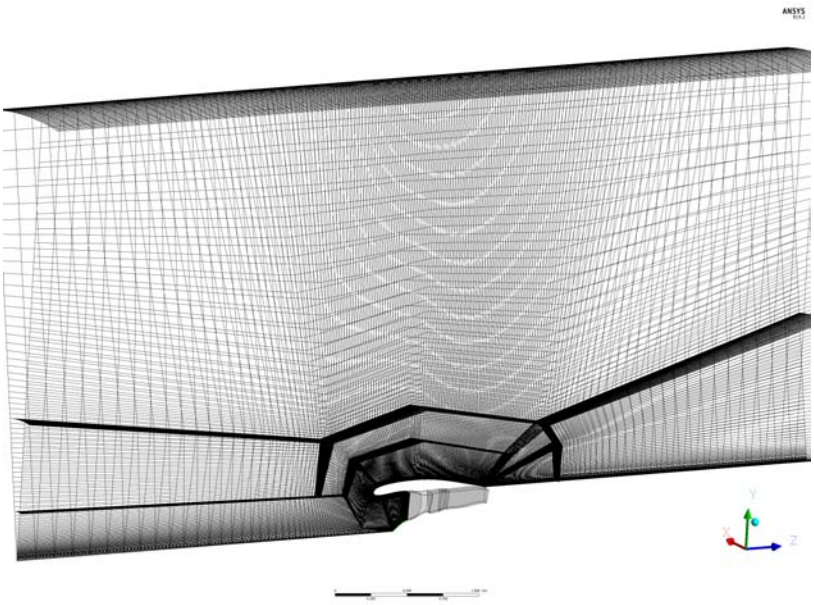

Figure 2.5: *3D view of Inner and Outer flow channel grid.*

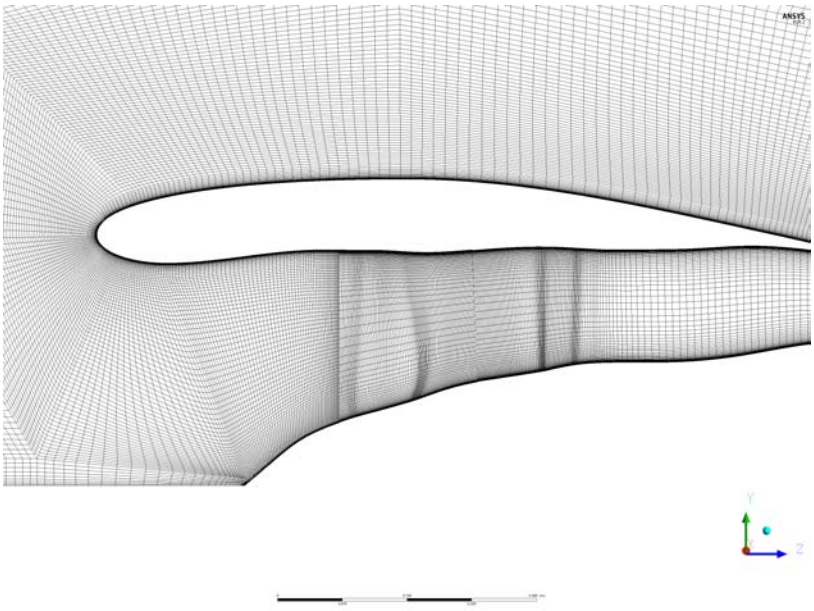

Figure 2.6: *2D view of Inner and Outer flow channel grid.*

2.2.3 Full-Annulus

This type of analysis considers an extra-coarse mesh to which the number of elements is slightly reduced up to 960528 for the passage of the inner channel. The external mesh was created starting by the mesh used in the simulation of Inner and Outer flow channel and reducing the number of its element from 2 million to 52000 for a single passage. The total

number of nodes of the external mesh for full annulus is 2334786. The difference between the number of external field elements in a single passage is certainly significant. The addition of the nacelle and the external fluid field is intended to recreate the conditions for the internal fan flow, so the loss of information in the external field description is widely accepted. Stators are also considered for the full-annulus simulation. Table 5 summarizes the dimensions of the various mesh domains adopted for this analysis.

Full-Annulus Mesh Domain	Number of Nodes	Passages
R1	21131616	22
S1	11253600	54
Outlet	4419360	54
External	2334786	45
Total Nodes	39139362	

Table 2.5: *Full-Annulus Mesh*

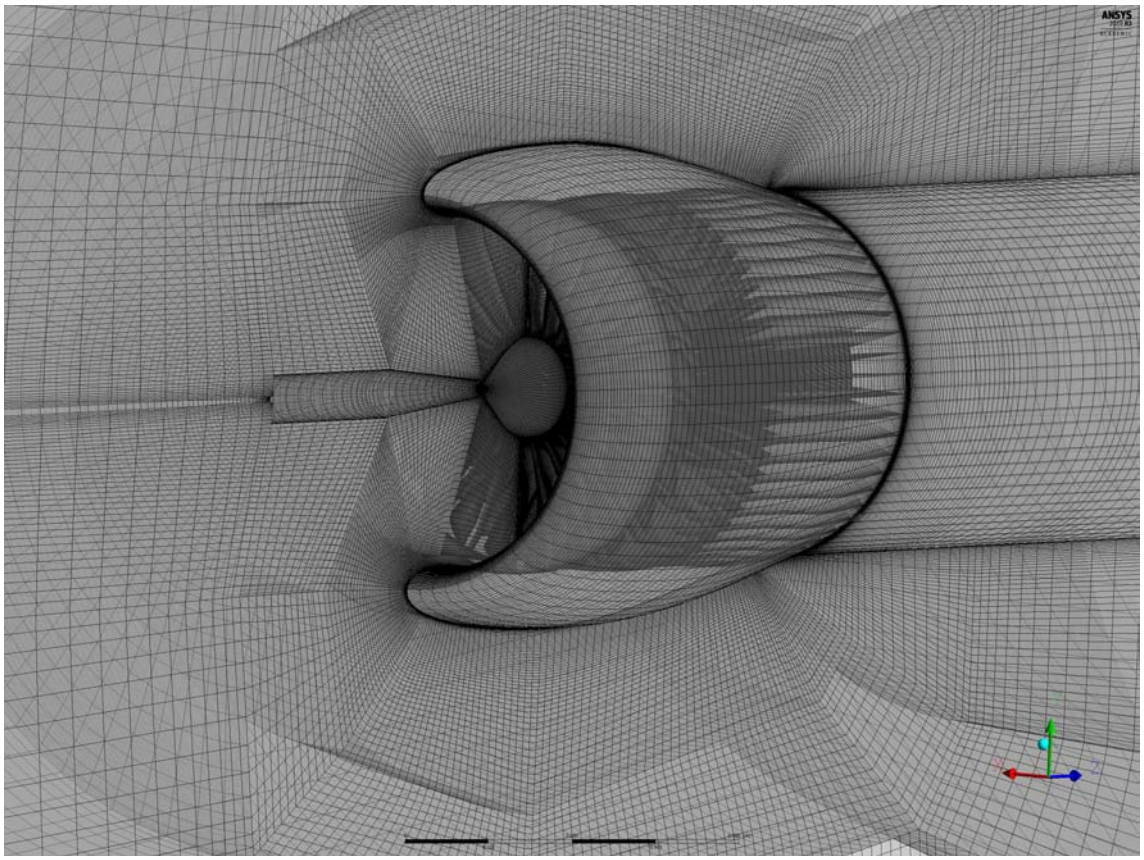

Figure 2.7: *Full-annulus mesh portion - 1*

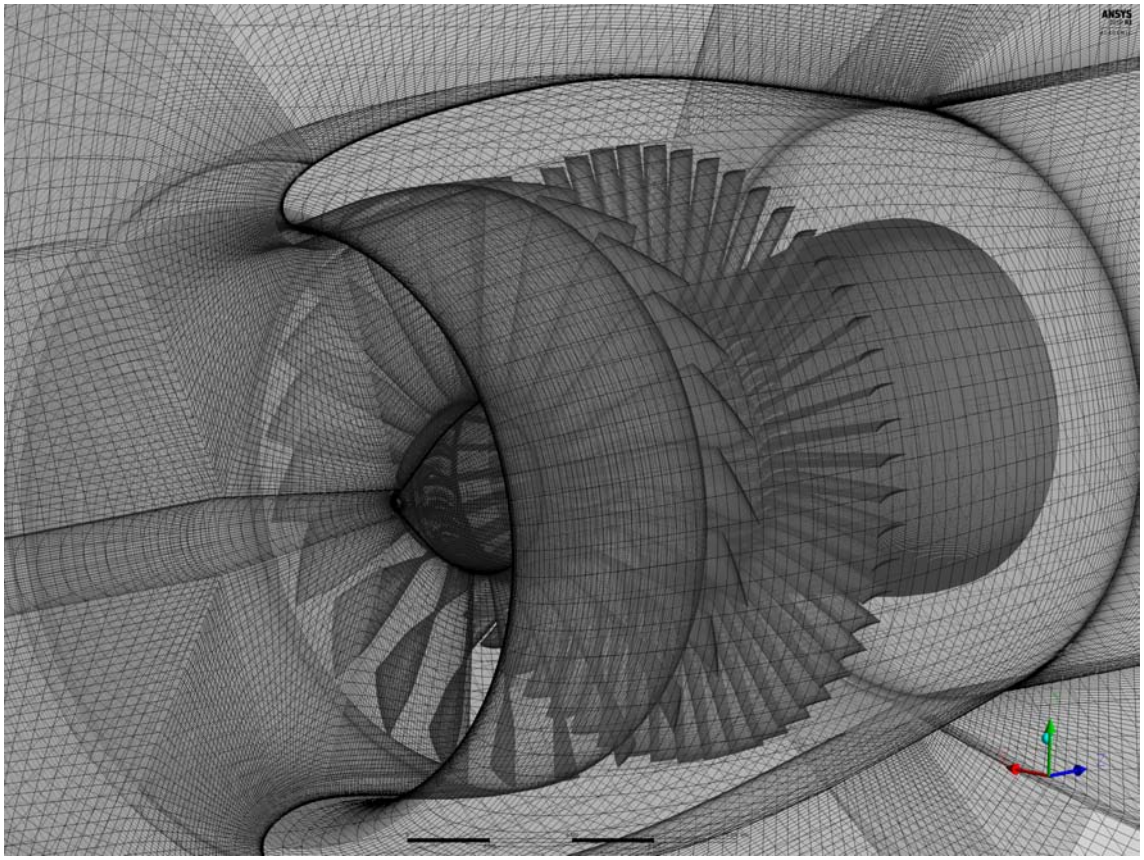

Figure 2.8: *Full-annulus mesh portion - 2*

2.3 Cfx - Pre

2.3.1 Turbulence models and Near wall treatment

CFD simulations carried out on Ansys (Cfx but also Fluent) are RANS simulations (Reynolds Average Navier-Stokes) or LES simulations (Large Eddy Simulation) which means that the real flow field is simulated by solving the mean flow field and the effect of turbulence is predicted with a mathematical model. In literature there are many of these models and in this thesis a macrocategory will be considered: the Eddy Viscosity Model and in particular the k-ω Shear Stress Transport and the k-ε RNG.
The k-ω SST model offers very precise predictions of the boundary layer separation due to adverse pressure gradients. The renormalized k-ε model (unlike the standard k-ε model which is based on a single turbulence length scale), redefines one of the constants in the

transport equation for the dissipation of turbulence. By means of this model, it is possible to take into account the different scales of motion through changes to the production term of the kinetic equation of the mean flow.
Another important aspect is the treatment of the near-wall region and how Cfx solves the boundary layer; infact there are two method for the wall treatment:

1 *Wall Function Method* uses empirical formulas (logarithmic relations) without solving the boundary layer. This method saves CPU time and reduces the size of the result file because a more coarse mesh is used near the wall.;

2 *Low-Reynolds Method*: this method is also known as Near Wall Model Approach and unlike the previous one not all turbulence model can be used. Only models based on the ω-equation are suitable for this approach, for example the SST model and the SMC (i.e. Second Moment Closure, not an Eddy viscosity Model but a Reynolds stress model) . In the Low-Reynolds method a very fine mesh is required because the boundary layer is solved, which means a very high CPU time.

Cfx ANSYS has developed the scalable wall function: in this method the wall functions are used as long as it is possible to switch to logarithmic approximation when the boundary layer is not completely solved. The transition between the two method occurs when the term y+ is greater than 11.06.
The k-ω SST turbulence model was adopted in the fine, medium, coarse and MEC_SST (i.e. Mesh Extra Coarse SST) while the k-ε RNG model was used for the MEC_RNG (i.e. Mesh Extra Coarse RNG) in order to compare the results obtained from these two meshes and understand which one was the most suitable for a full-annulus analysis.

2.3.2 Domain Interface

A steady-state simulation, requires management of the interface between the mobile reference frame and the fixed reference frame. Cfx allows to manage this interface using two option: Frozen Rotor or Stage Mixing-Plane. The Frozen Rotor option set a fixed relative orientation between the two frames and produce a steady-state solution: this model saves CPU computing time. The Stage Mixing-Plane is indicative for multi-stage compressors, the main idea unlike the previous one operates a circumferential average of the flows at the interface of the two reference systems. By producing a steady-state solution for both systems and then having to mix them in order to obtain a full stage solution, this approach is more time-consuming than the previous one.
All the simulations for the Inner Flow channel, have adopted the Frozen Rotor approach. In addition, some tests were carried out by implementing the Stage Mixing-Plane approach

based on the results of the Frozen Rotor approach and it was possible to observe that the solution is not significantly deviated. In the Single passage - Inner and Outer flow channel simulations and also in the Full-Annulus analysis the interface between domains was managed as follows:

- Stage Mixing-Plane for the interface between Rotor and Stator
- Frozen Rotor for all other interfaces

The use of the Frozen Rotor for the interface between the external domain and the rotor is justified by the fact that any distortions would be cancelled out by the Mixing-Plane.

2.3.3 Convergence strategy

All the simulations performed had an active control of the Timescale and the maximum number of iterations, specifically several simulations were made for each point of the fan map considering first a high number of maximum iterations and a very small Timescale 1E-6 and then gradually increasing it up to 1E-4. The active control of the characteristic quantities, i.e. mass flow rate, TPR, TTR and Adiabatic efficiency, allowed to understand when a simulation reached convergence. When these quantities stabilized for at least 200 iterations the simulation was considered finished and the next point of the fan map was reached. Each speed line was calculated from the chocking mass flow rate, this was useful to the solver and made it easier to calculate the solution as it was difficult to get mass flow returns from the outlet section. The next point of the fan map was reached modifying the boundary conditions for the Outlet and using as result the initialization file of the previous simulation. In this way it was possible to save a lot of CPU time.

2.3.4 Grid Convergenge Index

The GCI, as previously said, is used to estimate the discretization error in CFD simulation. This method is based on Richardson extrapolation and it is generally accepted within any paper review process. The recommended procedure begins by defining the grid size h for each mesh created

$$h_j = \left[\frac{1}{N_j} \sum_{i=1}^{N} (\Delta V_i) \right]^{1/3}$$

for j = 1, 2 and 3 where 1 is for Mesh fine, 2 for Mesh Medium and 3 for Mesh Coarse

so

$$h_1 < h_2 < h_3$$

Selecting a significant variable representative of the solution, in this thesis Adiabatic Efficiency was chosen. The next step is the calculation of apparent order p where

$$p = \frac{1}{\ln(r_{21})} |\ln |\varepsilon_{32}/\varepsilon_{21}| + q(p)|$$

$$\varepsilon_{32} = \phi_3 - \phi_2, \varepsilon_{21} = \phi_2 - \phi_1$$

where ϕ_k is the Adiabatic Efficiency of the kth grid.

$$q(p) = \ln\left(\frac{r_{21}^p - s}{r_{32}^p - s}\right)$$

$$s = 1 * sgn(\varepsilon_{32}/\varepsilon_{21})$$

Calculate the extrapolated values

$$\phi_{ext}^{21} = (r_{21}^p \phi_1 - \phi_2)/(r_{21}^p - 1)$$

Finally it is possible to calculate the following errors: Approximate relative error, the Extrapolated relative error and the Grid Convergence Index.

$$e_a^{21} = \left|\frac{\phi_1 - \phi_2}{\phi_1}\right|$$

$$e_{ext}^{21} = \left|\frac{\phi_{ext}^{12} - \phi_2}{\phi_{ext}^{12}}\right|$$

$$GCI_{fine}^{21} = \frac{1.25 e_a^{21}}{r_{21}^p - 1}$$

Similarly to a graph of an experimental measurement that is presented with the corresponding error bars, it is advisable to present a CFD simulation measurement with error bars that can be created with the GCI.

- III -

Simulation results

3.1 Fan performance

The first results that will be presented are the Fan maps obtained from the mesh sensitivity study simulating the Inner Flow channel. Figures 3.1, 3.2 and 3.3 show the results obtained with the three Mesh: Fine, Medium and Coarse for TPR TTR and Adiabatic Efficiency. The curves have a shape consistent with the curves of the experimental measurements, however it is observed that the data do not interpolate the test case curve but have a small offset, this phenomenon occurs for the Pressure and Temperature curves especially for the lower mass flow rates i.e. near the operating line.
All three meshes provide similar results, in fact the curves are very close to each other, but even the fine mesh cannot interpolate the experimental curve, therefore it can be assumed that it is not a mesh problem but something else.

Figures 3.4, 3.5 and 3.6 summarize the speedline tracking and compare them with the experimental measurement. Differences are highlighted especially for the estimation of the maximum efficiency point, simulations tend to overestimate it both in terms of mass flow and adiabatic efficiency. Some differences are also highlighted for the lower mass flow rates, in fact for them there is an underestimation of performance, similarly to what seen in the Take-off speedline. During the collection of the experimental data, in order to avoid too high stress on the rotor blade, the chocking condition was never reached, therefore it is not possible to compare the results obtained from the various simulations. All the points reported in the fan map have been obtained only by simulating the internal fluid dynamics of the turbofan, any differences with the experimental measurement may therefore partly depend on the model analyzed, however, it must be considered that the differences are relatively small.

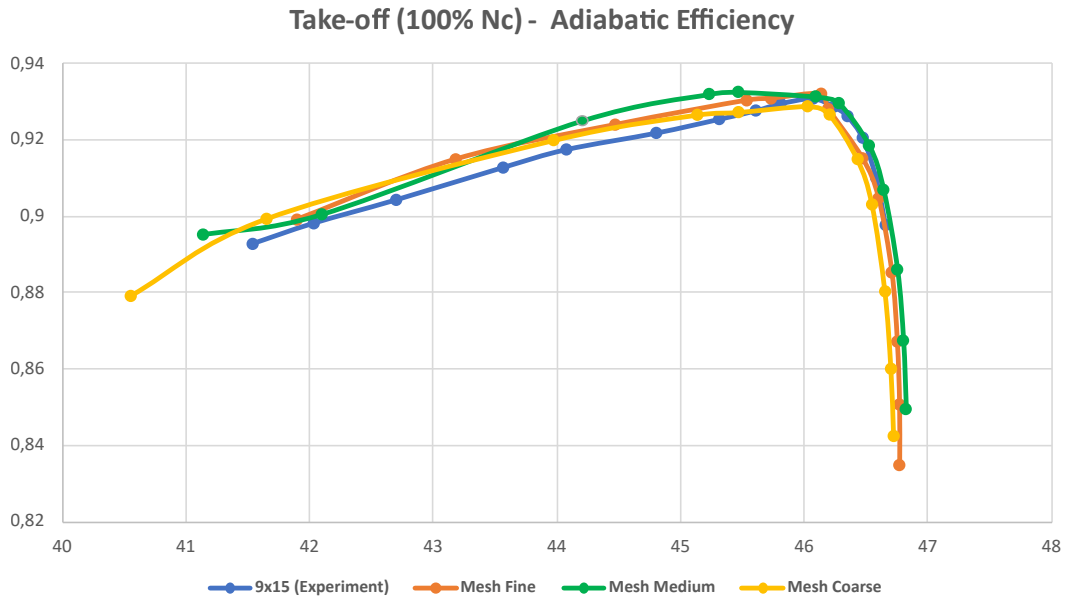

Figure 3.1: *Adiabatic Efficiency - Inner Flow channel simulations*

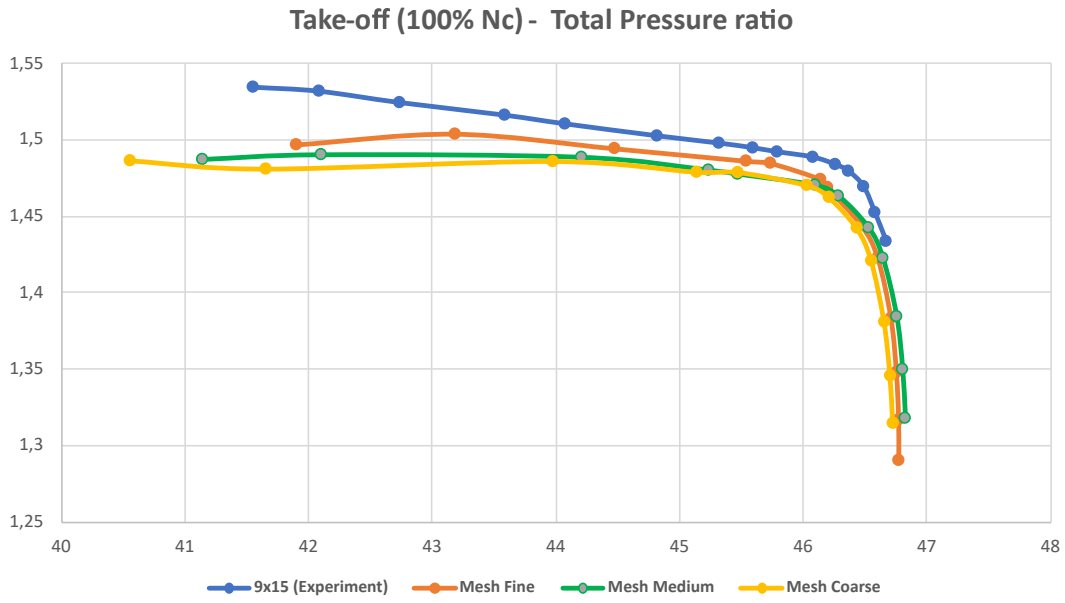

Figure 3.2: *Total Pressure ratio - Inner Flow channel simulations*

3.2 GCI: Grid Convergence Index

As explained in the previous chapter, thanks to GCI it is possible to create the error bars to be associated to the calculated adiabatic Efficiency, for example in figure 3.7 the errors between the fine mesh and the mesh medium (GCI_{21}) are shown.

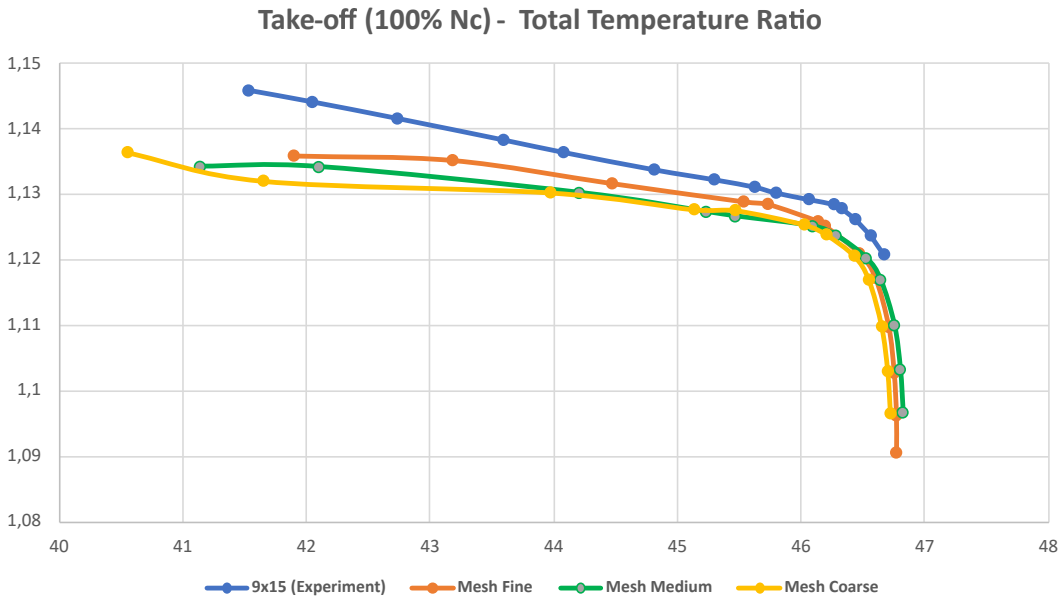

Figure 3.3: *Total Temperature ratio - Inner Flow channel simulations*

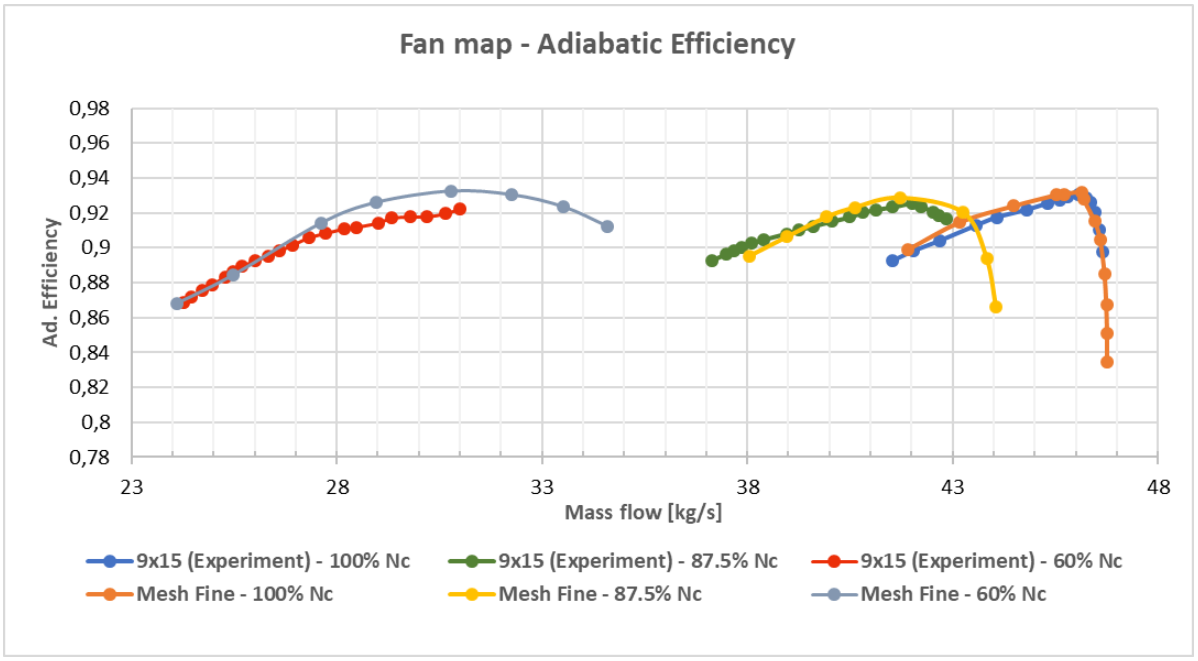

Figure 3.4: *Fan map - Adiabatic Efficiency - Inner Flow channel simulations*

3.3 Contour plot

In this section will be proposed Contour plots that compare the simulations results with the data obtained from LDV (Laser Velocimeter System and Data Acquisition). This device has been mounted in the test case described in [6].

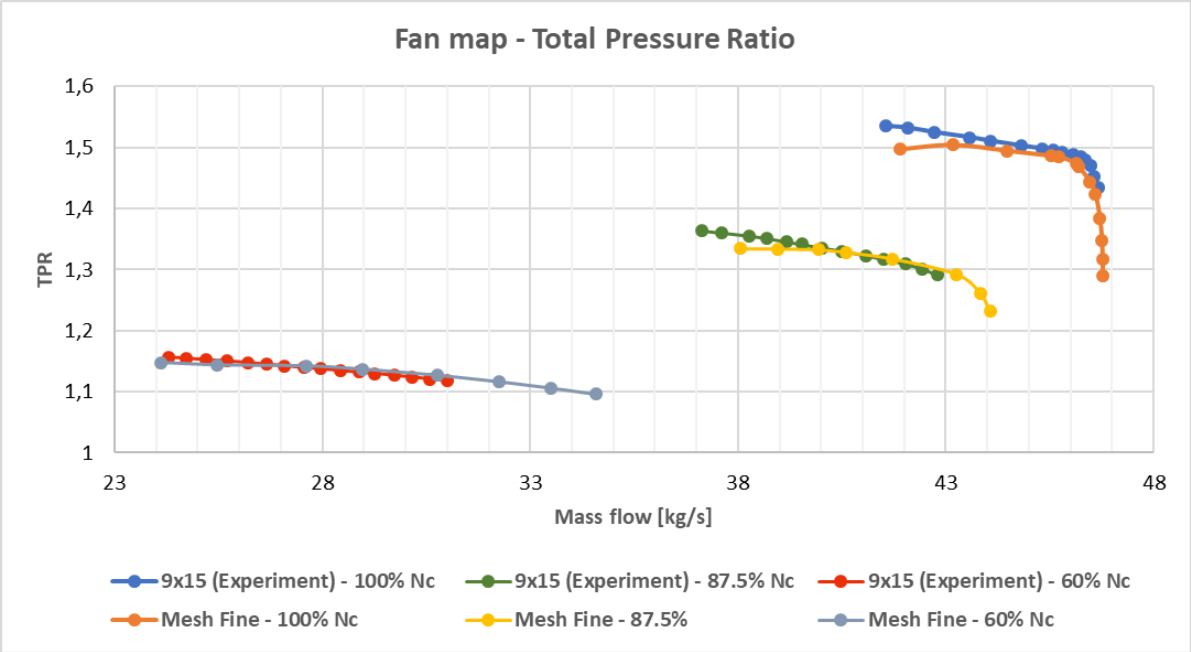

Figure 3.5: *Fan map - Total Pressure ratio - Inner Flow channel simulations*

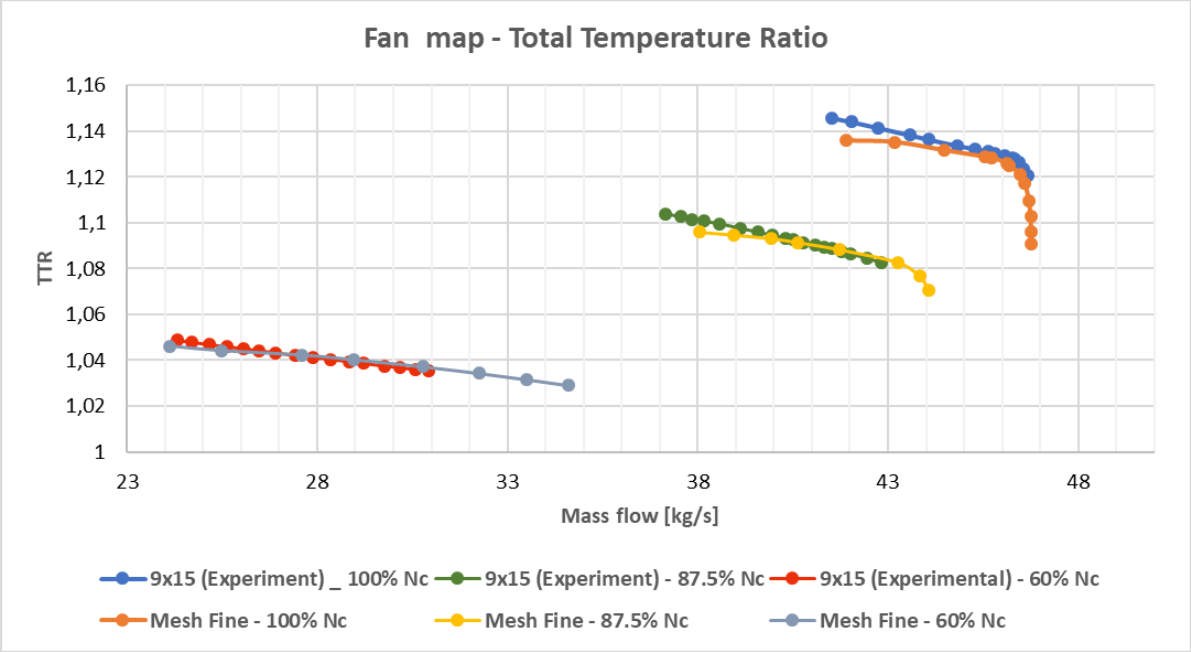

Figure 3.6: *Fan map - Total Temperature ratio - Inner Flow channel simulations*

The results refer to the Take-off speedline (12657 rpmc), and to highlight only the differences produced by the different discretization, the same pressure was taken at the outlet of the duct, i.e. 110000 [Pa] for all the meshes. Considering the same pressure may appear to be a wrong choice (from the fan maps it is clear that for the same exhaust pressures the points do not all fall at the same mass flow rate), therefore it follows that the calculated speed contours refer to different mass flow rates. The reference pressure was taken by

Mesh	Coarse	Medium	Fine					
p_{out} [Pa]	ϕ_3	ϕ_2	ϕ_1	ε_{32}	ε_{21}	s	$\ln\lvert\varepsilon_{32}/\varepsilon_{21}\rvert$	p
85000	0,842444	0,849494	0,850696	-0,007050	-0,001203	1	1,76837297	19,8966415
90000	0,859998	0,867399	0,867178	-0,007401	0,000221	-1	3,511468459	36,16159912
95000	0,880273	0,885974	0,885202	-0,005701	0,000772	-1	1,9998928	19,44645945
100000	0,903016	0,906865	0,904666	-0,003848	0,002199	-1	0,559727907	4,078976154
102500	0,914871	0,918465	0,915115	-0,003594	0,003350	-1	0,070428108	4,600425034
105000	0,926535	0,929536	0,928060	-0,003001	0,001476	-1	0,709381395	5,36837157
106000	0,928752	0,931283	0,931980	-0,002531	-0,000697	1	1,290382466	15,63683166
107500	0,927195	0,932503	0,930776	-0,005308	0,001727	-1	1,122692982	9,436268329
108000	0,926523	0,931972	0,930287	-0,005449	0,001685	-1	1,173789774	9,986054303
110000	0,919851	0,924998	0,923893	-0,005147	0,001104	-1	1,5394096	14,10706231
112500	0,899268	0,900422	0,914844	-0,001154	-0,014422	1	-2,525836312	6,118701039
113500	0,879064	0,895144	0,899075	-0,016080	-0,003931	1	1,408696281	16,66475842

Table 3.1: *GCI part 1*

p_{out} [Pa]	ϕ_{ext}^{21}	e_a^{21}	e_{ext}^{21}	GCI_{fine}^{21}	ϕ_{ext}^{32}	e_a^{32}	e_{ext}^{32}	GCI_{fine}^{32}
85000	0.850714	0.001414	0.000020	0.000025	0.850711	0.008299	0.001431	0.001791
90000	0,867178	0,000255	0,000000	0,000000	0,867634	0,008532	0,000271	0,000338
95000	0,885190	0,000872	0,000014	0,000017	0,887010	0,006435	0,001168	0,001462
100000	0,903089	0,002431	0,001746	0,002178	0,914865	0,004244	0,008745	0,011028
102500	0,913119	0,003660	0,002187	0,002727	0,924915	0,003913	0,006973	0,008778
105000	0,927375	0,001591	0,000738	0,000922	0,933971	0,003229	0,004748	0,005964
106000	0,932005	0,000747	0,000027	0,000034	0,932005	0,002718	0,000775	0,000969
107500	0,930512	0,001856	0,000284	0,000355	0,936088	0,005692	0,003830	0,004806
108000	0,930062	0,001811	0,000242	0,000303	0,935345	0,005847	0,003606	0,004524
110000	0,923837	0,001195	0,000061	0,000077	0,926779	0,005564	0,001922	0,002407
112500	0,920173	0,015764	0,005791	0,007281	0,901860	0,001281	0,001594	0,001996
113500	0,899189	0,004372	0,000127	0,000159	0,899189	0,017964	0,004499	0,005649

Table 3.2: *GCI part 2*

looking at the results of the fine mesh, consequently any errors on the mass flow rate are to be attributed solely to the more coarse discretization. Studying different meshes with the same boundary condition one denotes how much it is possible to reduce the number of elements and especially which areas are more critical.

To make comparison with the experimental data easier, the Cfx - Post option was used, which graphically multiplies the results obtained from a single passage analysis. Since this is a post processing operation, it is good to remember that the full-annulus result thus obtained has no value. The only result to be considered valid as it is calculated numerically is the single passage result.

Observing the images of figure 3.8 it is possible to make some preliminary considerations: by decreasing the number of elements, the result is particularly affected in the wakes that in the axial velocity plots are represented as much larger than in the experimental measurement. An observation that concerns all meshes is the bad prediction for the area near the blade tip where the calculated axial speeds are much lower than those measured.

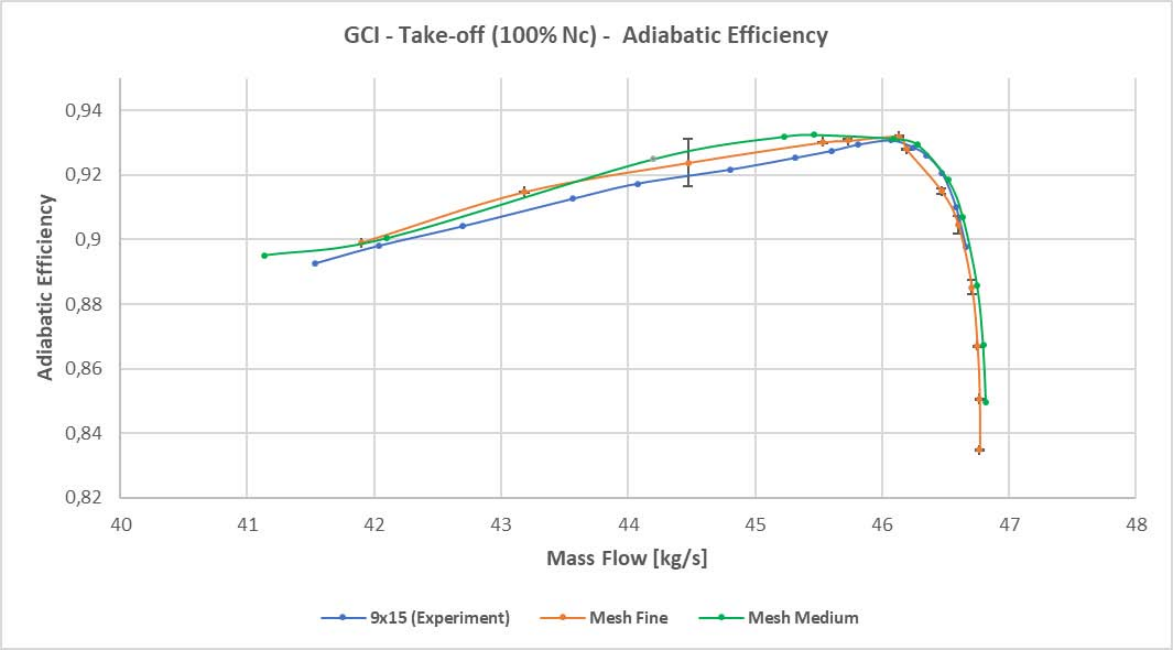

Figure 3.7: *Fan map - Adiabatic Efficiency - Take-off speedline - GCI*

From the Circumferential Velocity plots instead it is possible to observe how the zone near the hub is much less homogeneous as the number of mesh elements decreases. The experimental measurement instead shows an almost uniform velocity zone and certainly does not have zones of low velocity so large up to the hub as reported for example by the simulation with the mesh coarse.

3.4 Spanwise profile

The test case reports also provide spanwise profiles of some characteristic quantities such as total pressure ratio and adiabatic efficiency. These data, in addition to the fan map, were used to validate the CFD model and understand which areas were well described and which required a different treatment in terms of mesh density, boundary conditions and turbulence model. In addition to the profile graphs along the span, a further comparison was made considering the contour plots of the Mach number in three spanwise positions (i.e. Near Hub 11%,Near Mid 51%, Near Tip 89%) provided by the report of the CFD model developed by NASA. It was possible to make a comparison even to 94% of the span using a contour plot provided in the SDT.A

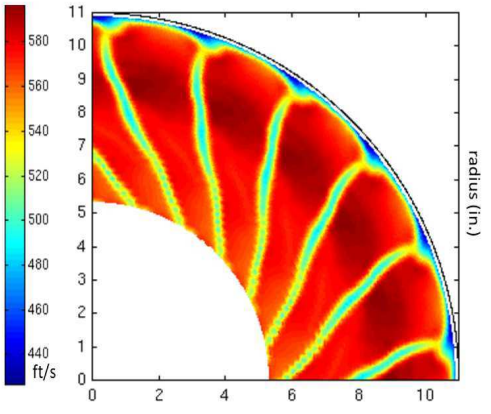

(a) *Measured by LDV*

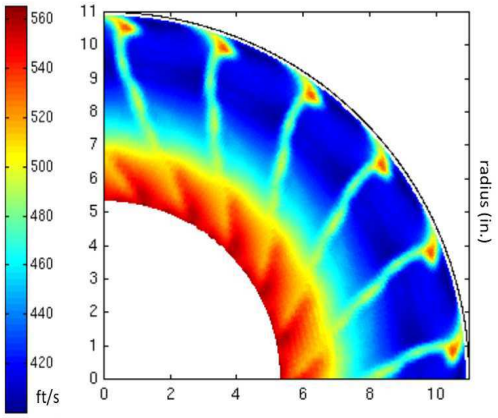

(b) *Measured by LDV*

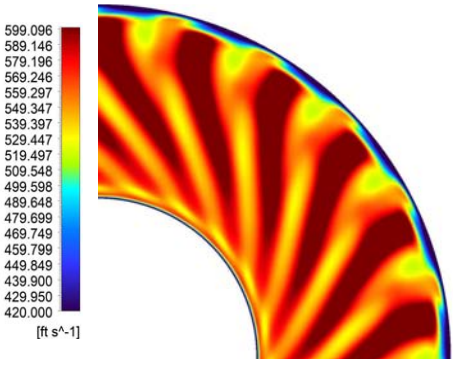

(c) *Mesh Fine*

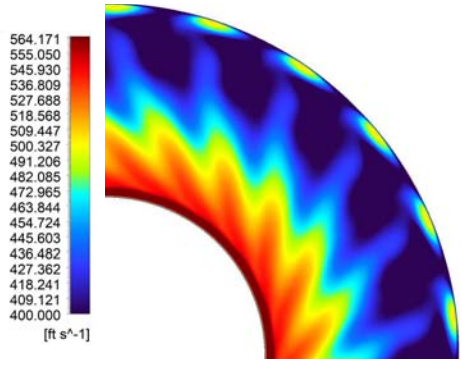

(d) *Mesh Fine*

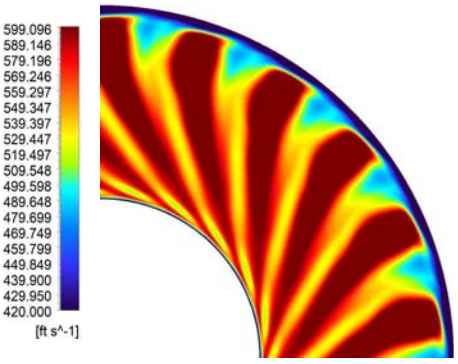

(e) *Mesh Medium*

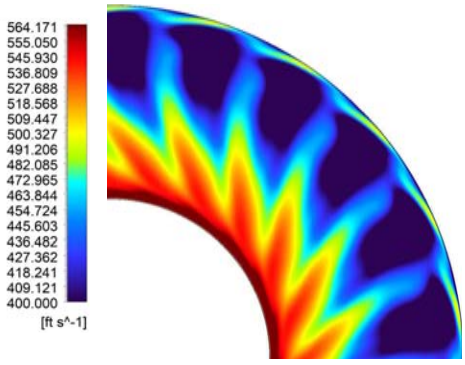

(f) *Mesh Medium*

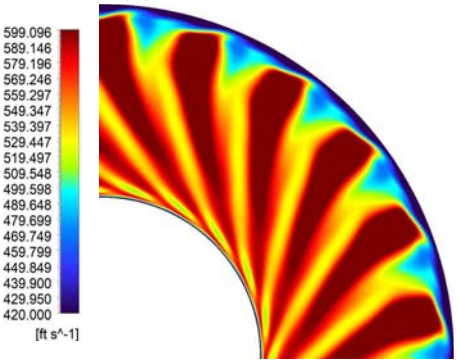

(g) *Mesh Coarse*

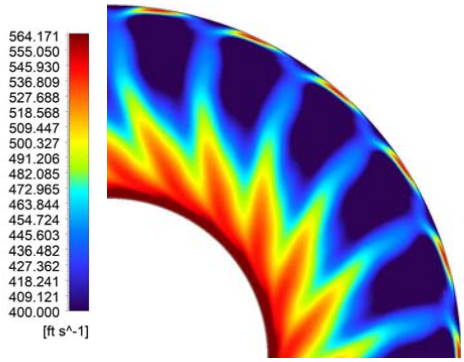

(h) *Mesh Coarse*

Figure 3.8: *Contour plot of Axial Velocity (Sx) and Circumferential Velocity (Dx) - Take-off speedline - Inner Flow Channel*

3.4.1 Contour Plot - Relative Mach number

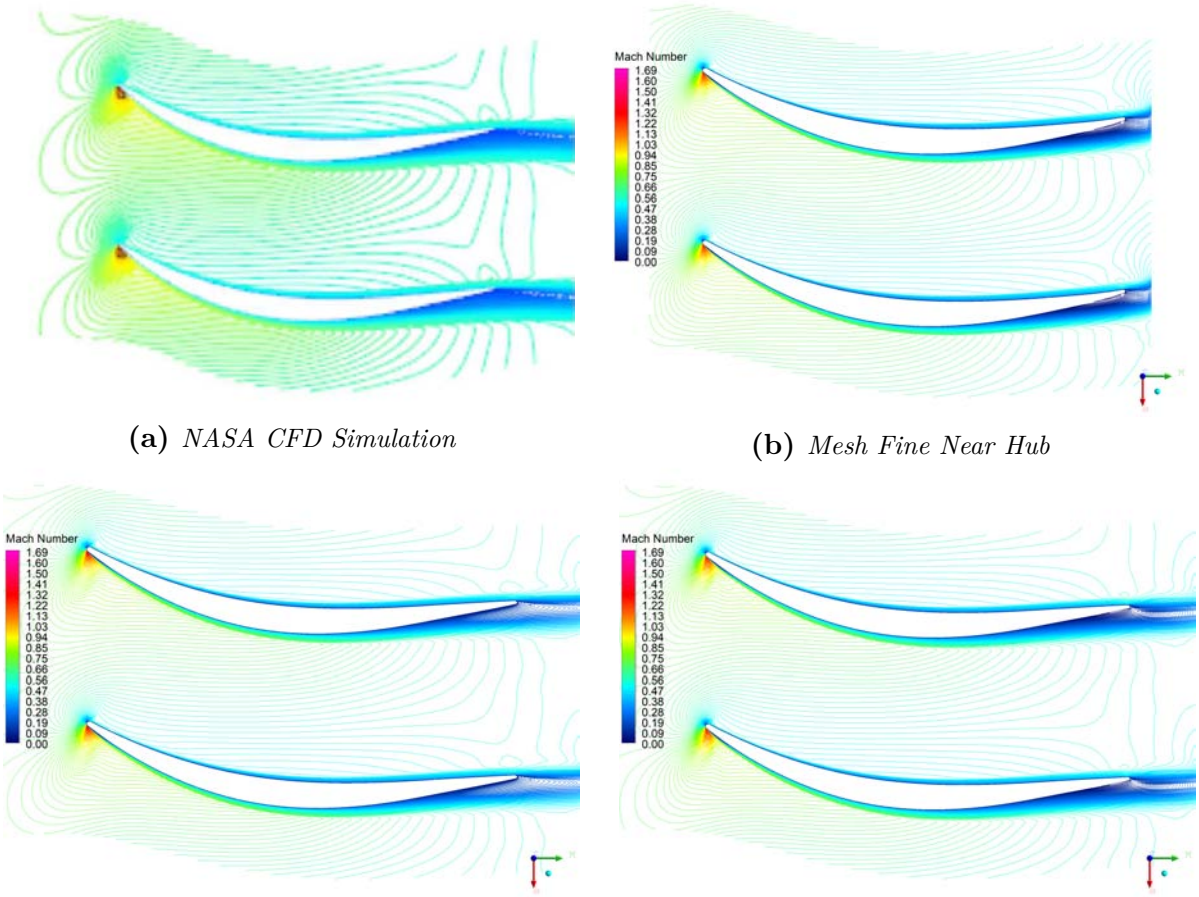

(a) *NASA CFD Simulation*

(b) *Mesh Fine Near Hub*

(c) *Mesh Medium Near Hub*

(d) *Mesh Coarse*

Figure 3.9: *Contour plot of relative Mach Number Near Hub - Take-off speedline - Inner Flow Channel*

Each contour plot in figure 3.9, 3.10 and 3.11 shows two blades, but this is only the graphic repetition that can be done in CFD post. As you can see, the flow at the Leading Edge is well described by all the meshes, but it is not the same for the interface between the two blades and the wake. It can also observe different distributions of the Mach number probably due to the management of the number and the distribution of the elements near the walls of the channel.
The CFD simulation developed by NASA in fact uses a structured mesh type H-O-H unlike the one implemented in Cfx so this different approach can lead to some differences in the description of the flow field.

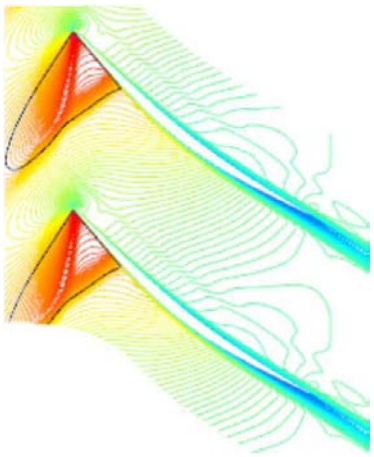

(a) *NASA CFD Simulation*

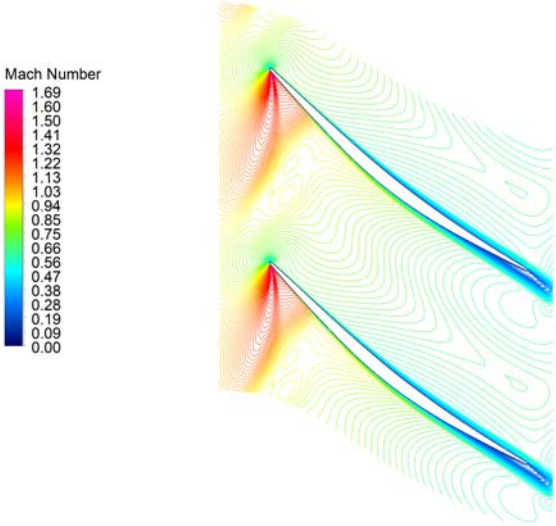

(b) *Mesh Fine Near Hub*

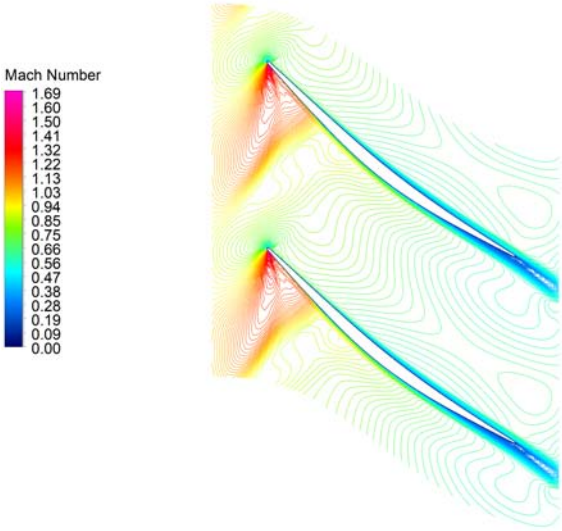

(c) *Mesh Medium Near Hub*

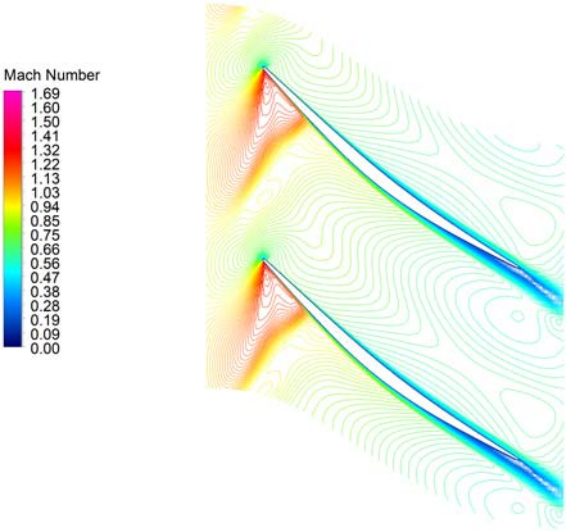

(d) *Mesh Coarse*

Figure 3.10: *Contour plot of relative Mach Number Near Mid - Take-off speedline - Inner Flow Channel*

As the span increases, there is a worse description of the Mach number, similarly to the axial and circumferential velocity contour plots where the Tip region reported values very different from those of the experimental measurement. It should be noted however that the simulations made with the various meshes do not give very different results, this suggests that it is not a coarse mesh error but to be attributed to something else.

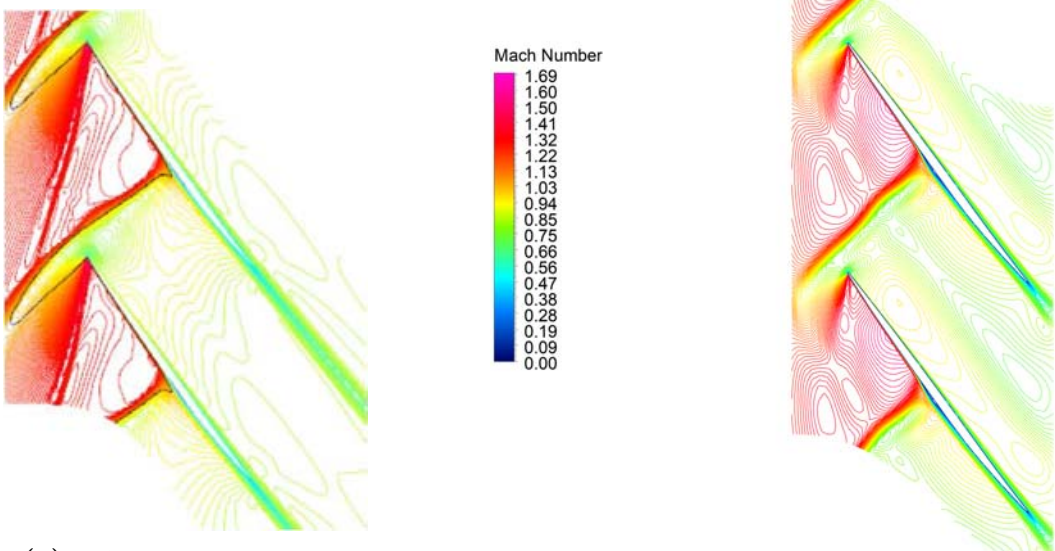

(a) *NASA CFD Simulation*

(b) *Mesh Fine Near Hub*

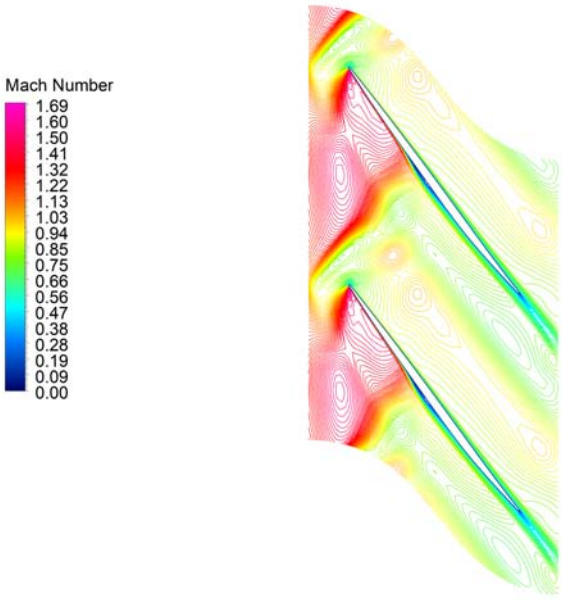

(c) *Mesh Medium Near Hub*

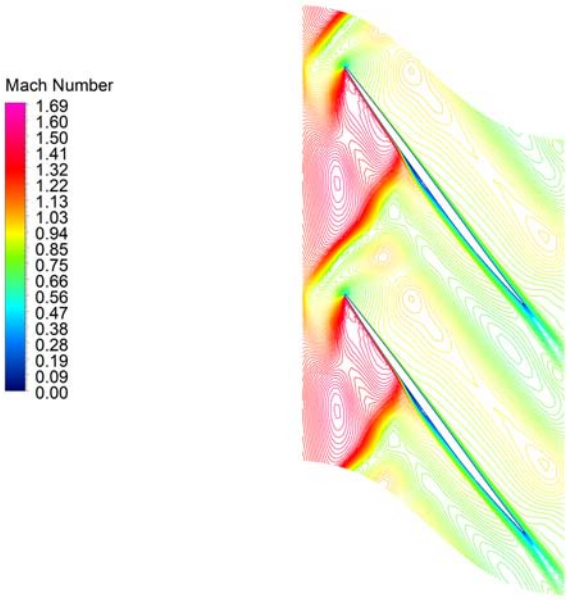

(d) *Mesh Coarse*

Figure 3.11: *Contour plot of relative Mach Number Near Tip - Take-off speedline - Inner Flow Channel*

3.4.2 Total Pressure Ratio and Adiabatic Efficiency

Figure 3.12 shows TPR's long span profiles and adiabatic efficiency. It can be seen that from 50% of the blade to the tip, each simulation regardless of the mesh used, badly

interpolates the experimental measurement.

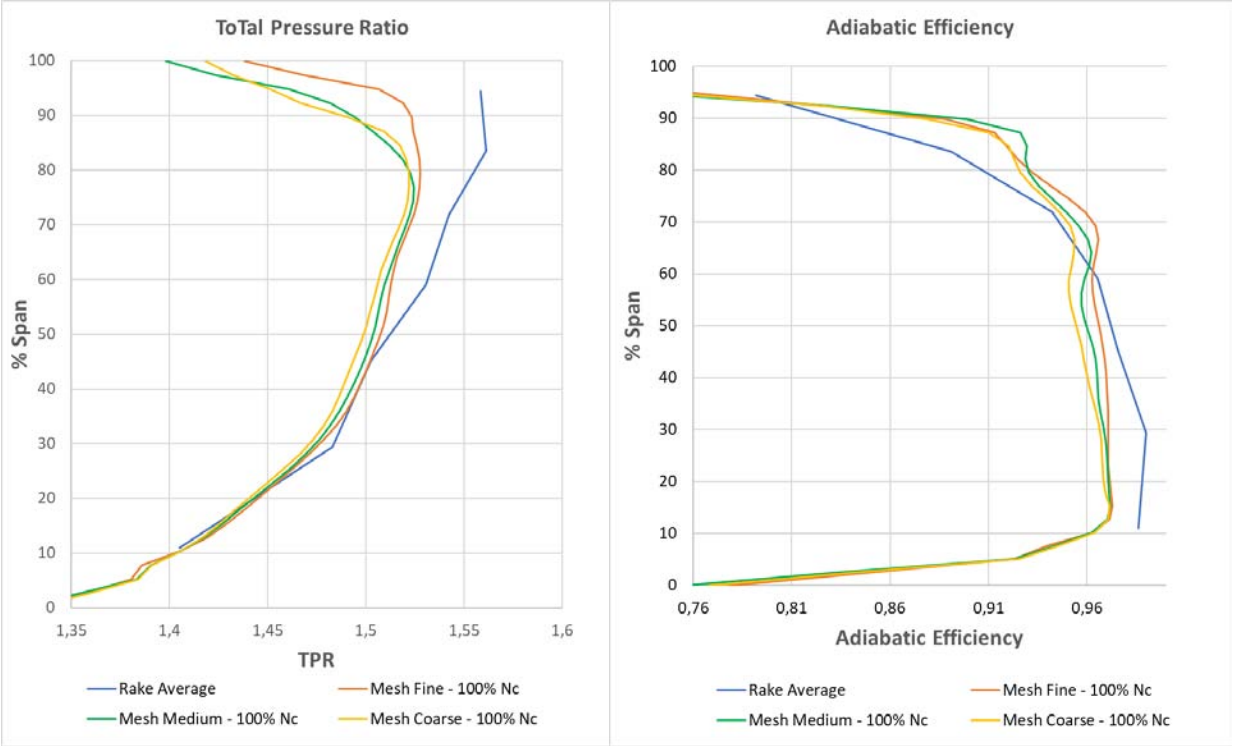

Figure 3.12: *Spanwise profile: TPR (Sx),Adiabatic Efficiency (Dx) - Take-off speedline*

Although the simulation does not approach the experimental measurement, this graph shows that the curves calculated by the different meshes are very close to each other. Starting from this consideration the two Extra Coarse meshes have been created. As already explained above, as well as having a smaller number of elements than the coarse mesh are arranged differently. A greater number of elements has been used for the wake decreasing those at the inlet, using also different turbulence models has required to modify the boundary layer treatment. The analysis for these two meshes have been particularly fast because the solution has been initialized starting from the results obtained from the fine mesh thus reducing the CPU time.
Below are the results of the spanwise profiles obtained from the analysis of the Extra coarse mesh compared with those of the experimental measurement and the Mesh Fine, however, there are no particular improvements in the solution in fact the Tip is still poorly described.

The solutions obtained with these two new meshes are very close to those obtained with the previous meshes, although there is a slight improvement in the TPR system by the MEC_RNG mesh in the blade section from 50% to 80%. Near the tip instead the result is much worse than the previous cases for both extra coarse meshes. This analysis made it possible to assume that the drop in performance near the tip is not due to a too

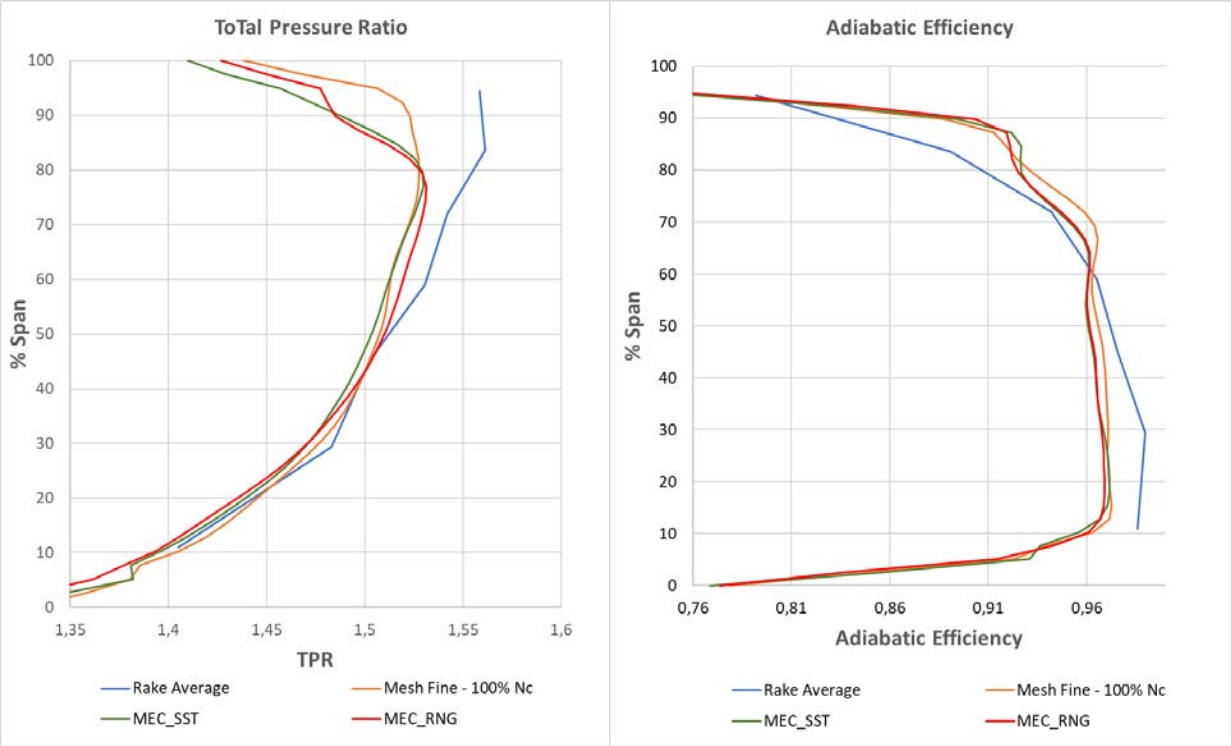

Figure 3.13: *Spanwise profile obtained with the Extra coarse meshes: TPR (Sx),Adiabatic Efficiency (Dx) - Take-off speedline.*

coarse mesh or even to the turbulence model used. The Contour plot of the Mach number in the three position of the span, the Axial and Circumferential velocities obtained for the Extra coarse meshes are shown in Appendix A.

3.5 Inner and Outer results

The results reported up to this point presented some problems, the most evident one regards the description of the flow near tip as indicated in the spanwise profile and in the contour plot of velocity component. Modeling the fan with his own nacelle and also considering the external domain has improved the solution obtained from all the cases reported so far, the most significant are the spanwise profiles of TPR and Adiabatic Efficiency.

Figure 3.14 compares the results previously obtained with those of the simulation with nacelle and external domain. As can be seen, TPR's profile is extremely well interpolated. Further differences can be observed also in the velocity patterns as shown in figure 3.15, the circumferential velocity component is pretty closer to the experimental result specifically between hub and mid region. The axial velocity component also shows some differences

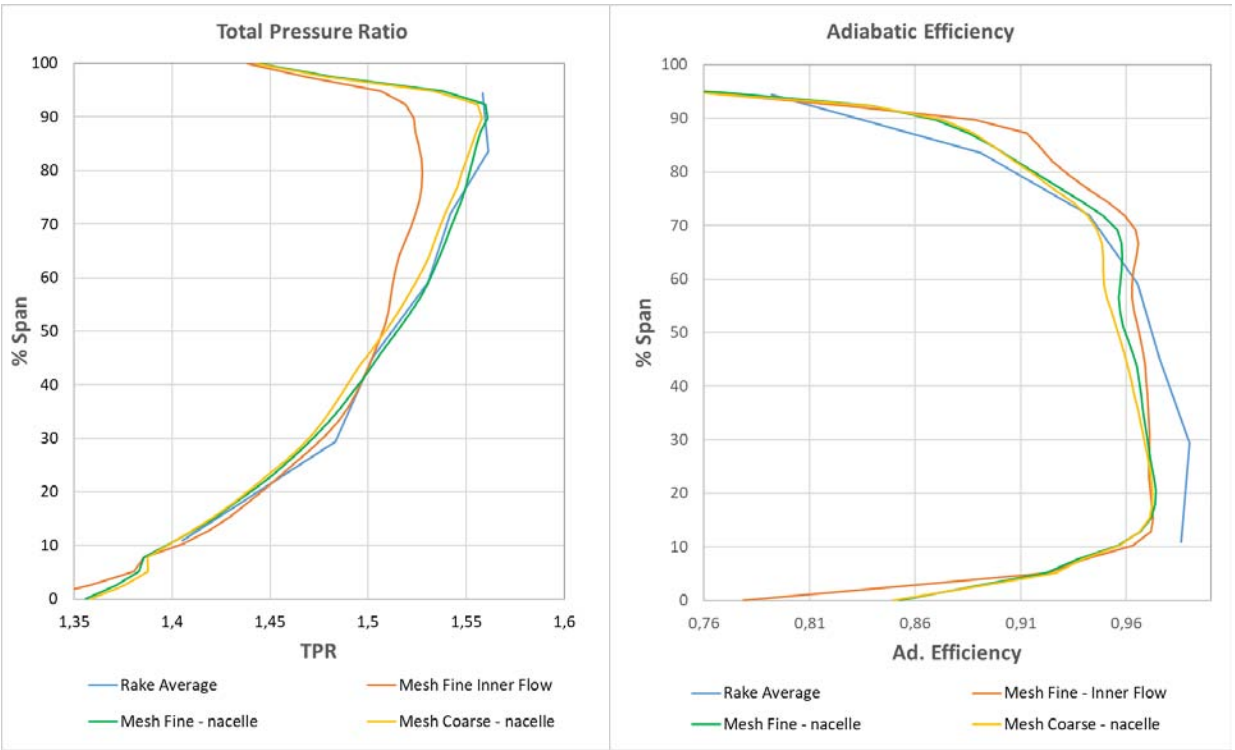

Figure 3.14: *Spanwise profile obtained with the Inner and Outer Flow channel: TPR (Sx),Adiabatic Efficiency (Dx) - Take-off speedline.*

compared to the previous cases, a low speed zone formation is observed between two adjacent wakes.

The reason of these different behaviors may be that the images of the velocity components were not captured by the Fan in nacelle configuration but with a Bellmouth inlet as described in the SDT test case [6]. The simulations analyzed made it possible to highlight the relationship between intake and the behavior near the blade tip. The analysis of the intubated fan evidently simulated an inlet more similar to the bellmouth and consequently the resulting velocity pattern was very similar. The fan simulation with the intake, especially in take-off condition, is affected by the deformation of the streamlines thus modifying the upstream input conditions and consequently the performance and fluid dynamics downstream of the rotor. An accurate comparison with experimental velocity measurements should be made by simulating the bellmouth inlet adopted in the NASA test case.

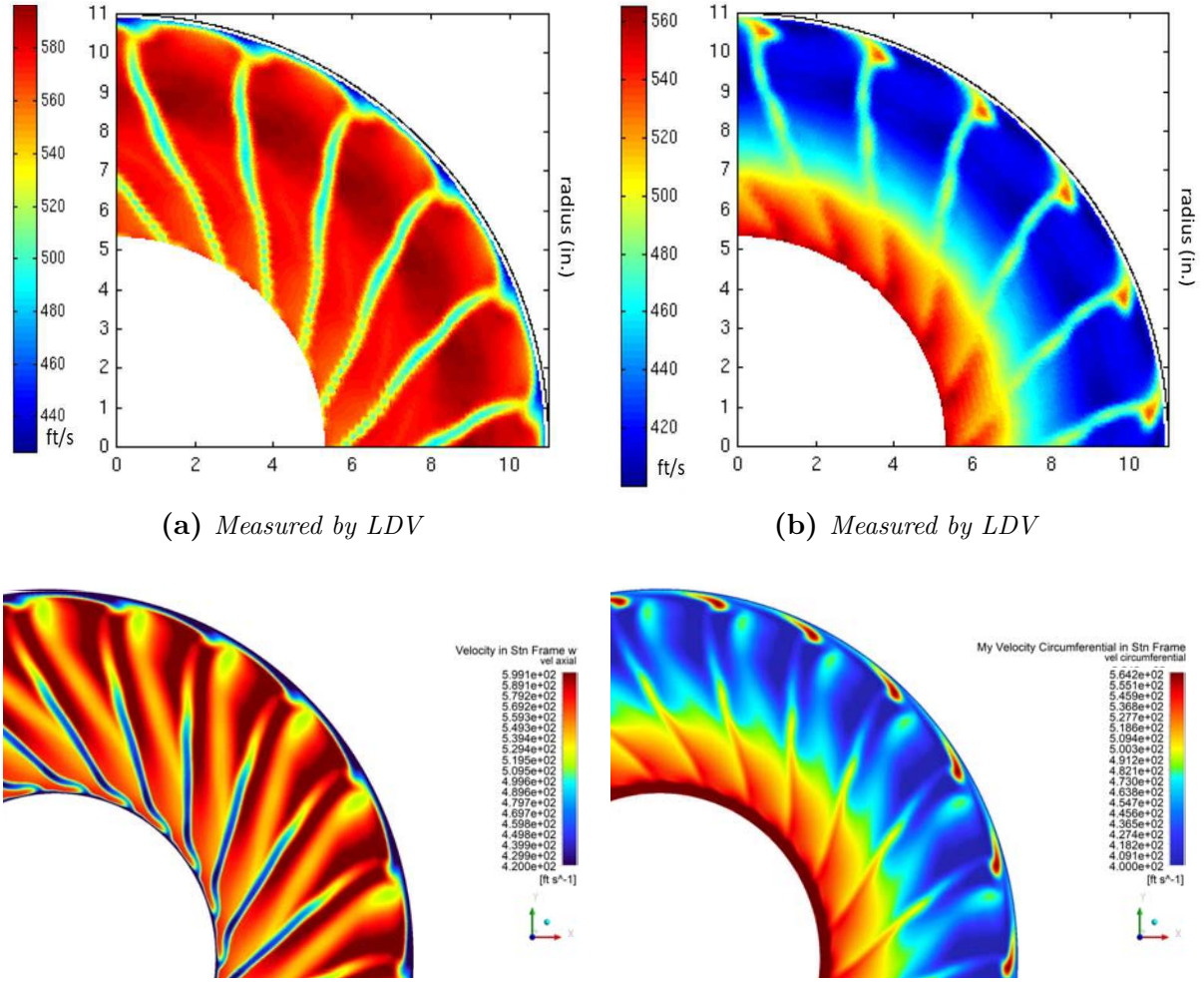

(a) *Measured by LDV*

(b) *Measured by LDV*

(c) *Mesh Fine - Nacelle - Axial Velocity*

(d) *Mesh Fine - Nacelle - Circumferential Velocity*

Figure 3.15: *Experimental Measure VS Inner and Outer flow channel - Contour plot - Velocity component - Take-off speedline*

3.5.1 Contour plot - Relative Mach number

In figure 3.16 it is possible to notice the improvement in the description of the fluid flow field, in particular for the position of the shock wave. The contour plots used as reference to validate the solution come from NASA's CFD simulation where the fluid channel was simulated with its nacelle. The analogy found between the two simulations is further proof that the differences previously found were due only to the lack of external domain.

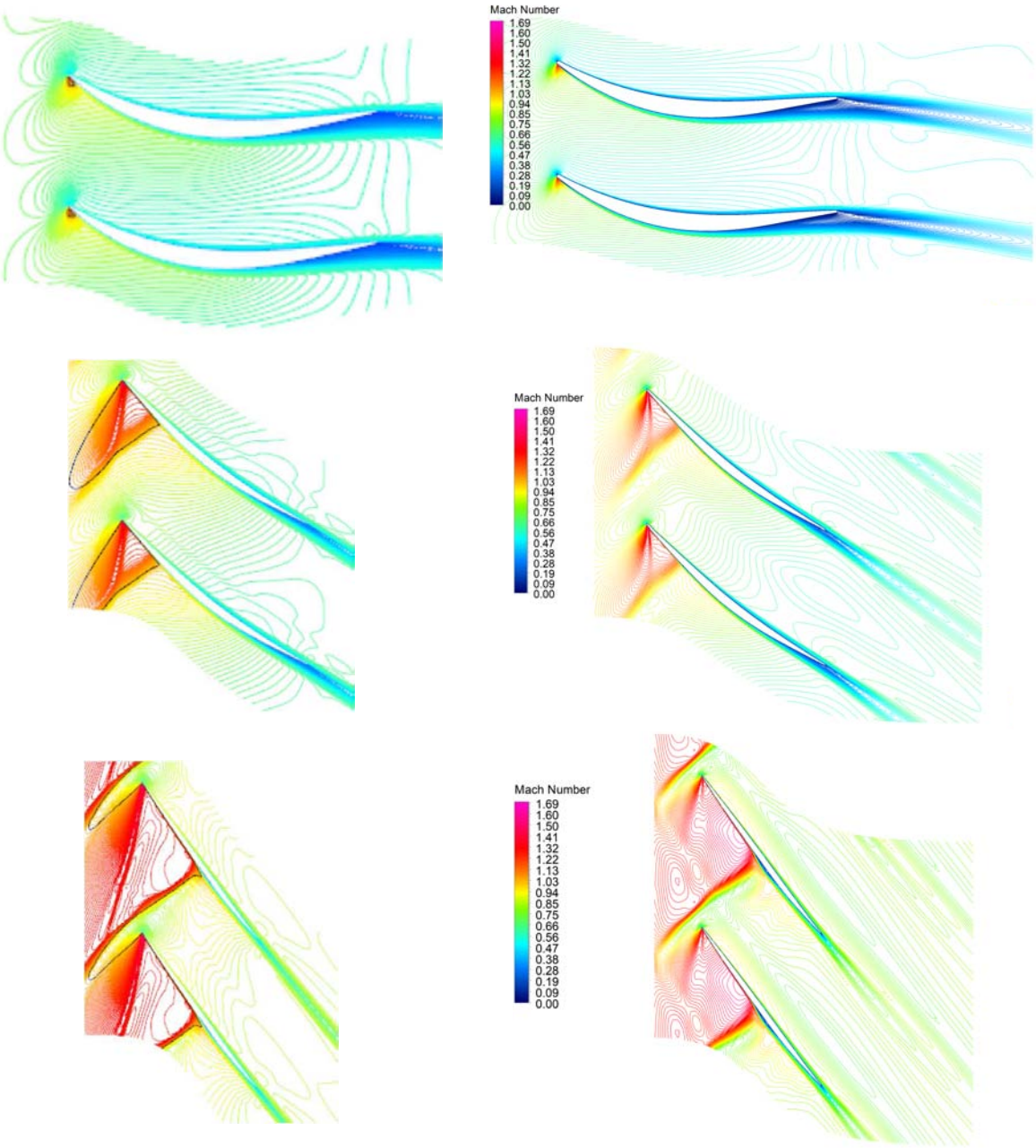

Figure 3.16: *Contour plot of relative Mach Number Near Tip - Take-off speedline - Fan with his own nacelle*

3.5.2 Fan map

The last aspect to consider is the fan map. Other points of the speed line are also reported but are not comparable with the experimental measurement because the map was drawn using VFEN. The geometry of the channel used refers only to the operating point of the 100% speedline. However, it can be observed that the operating point is very close to the

TPR and TTR curves.

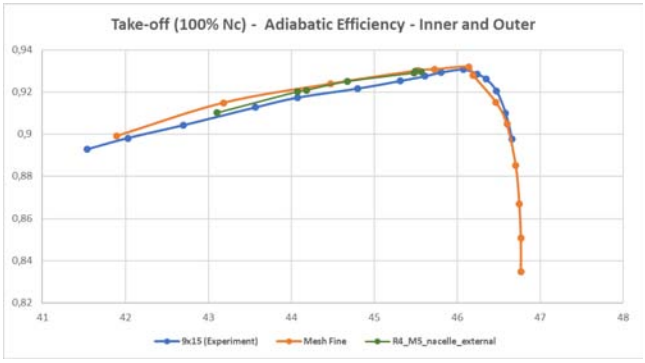

Figure 3.17: *Adiabatic Efficiency - Inner and Outer Flow channel simulations*

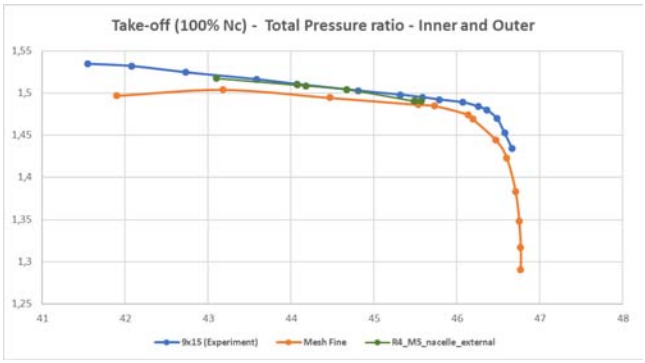

Figure 3.18: *Total Pressure ratio - Inner and Outer Flow channel simulations*

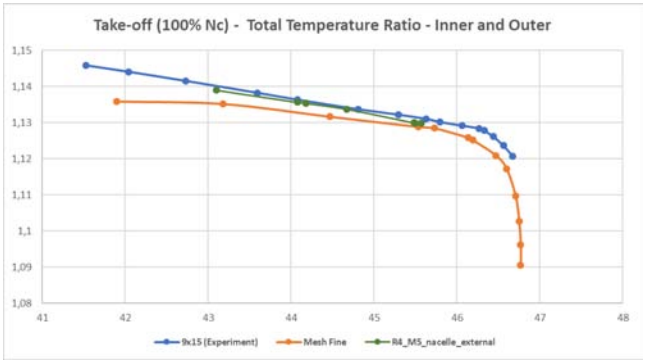

Figure 3.19: *Total Temperature ratio - Inner and Outer Flow channel simulations*

In conclusion, the results obtained with the simulation in single passage with nacelle and external domain have satisfied the requirements. The model validated has been multiplied in circumferential direction creating the complete model for the Full-annulus analysis.

3.6 Full-Annulus

In this chapter are reported all the results obtained from the Full-Annulus analysis. The figure 3.20 shows the comparison between the result obtained by the post processing of the Single passage analysis (Internal and External field) and the results of the Full Annulus analysis. Thanks to this comparison, the differences between the circular repetition of the solution and the real calculated are highlighted. In the proximity of the tip it is possible to observe that in both Contour Plots the high speed bubbles obtained from the Single Passage analysis are mitigated. Having imposed the same boundary conditions on the system, it is possible to declare that the solution of the single passage presents evident simplifications due to the imposition of the periodicity.

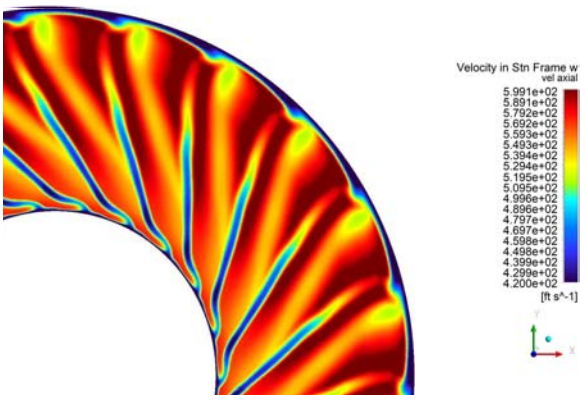

(a) *Mesh Fine - Nacelle - Axial Velocity*

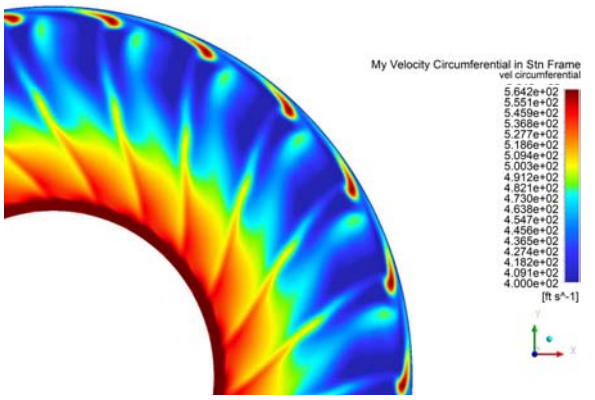

(b) *Mesh Fine - Nacelle - Circumferential Velocity*

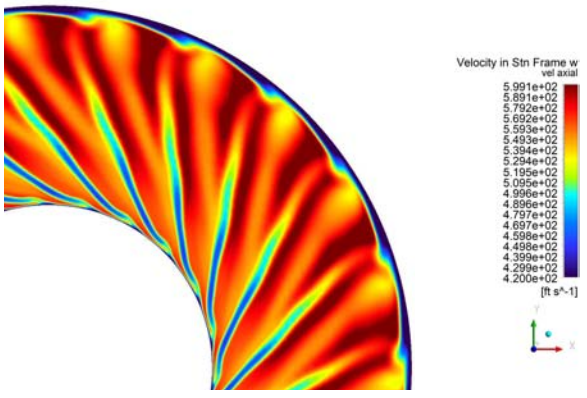

(c) *Full-Annulus Mesh portion - Axial Velocity*

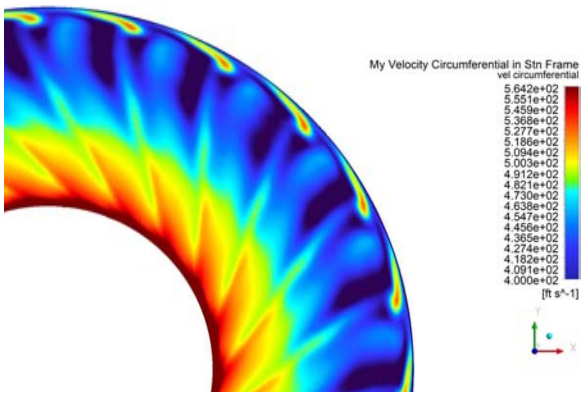

(d) *Full-Annulus Mesh portion - Circumferential Velocity*

Figure 3.20: *Inner and Outer flow channel VS Full-annulus - Contour plot - Velocity component - Take-off speedline*

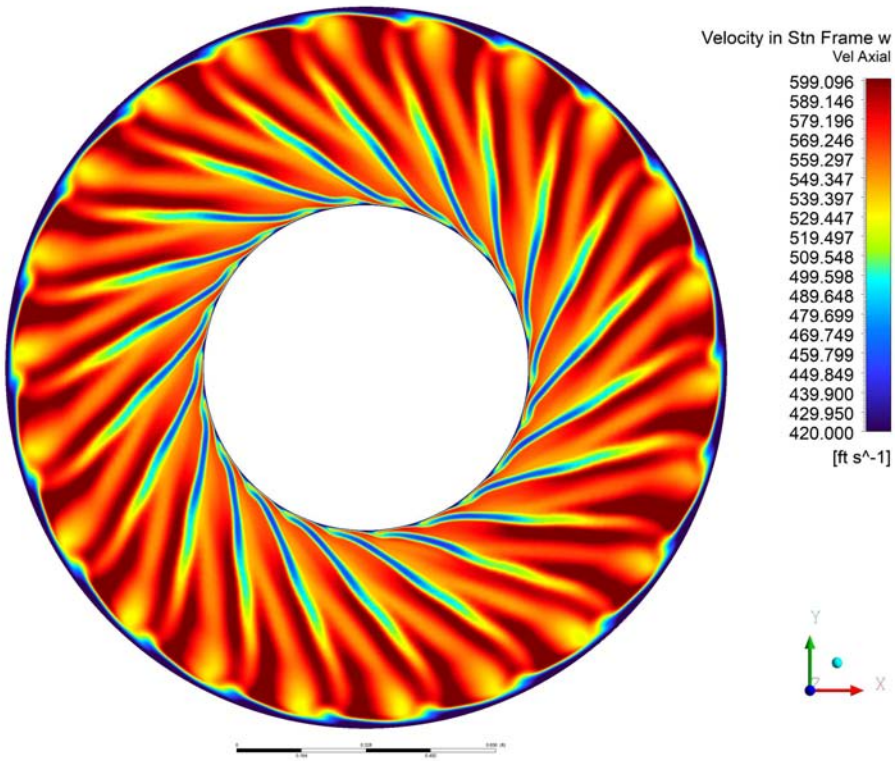

Figure 3.21: *Full-Annulus - Axial Velocity*

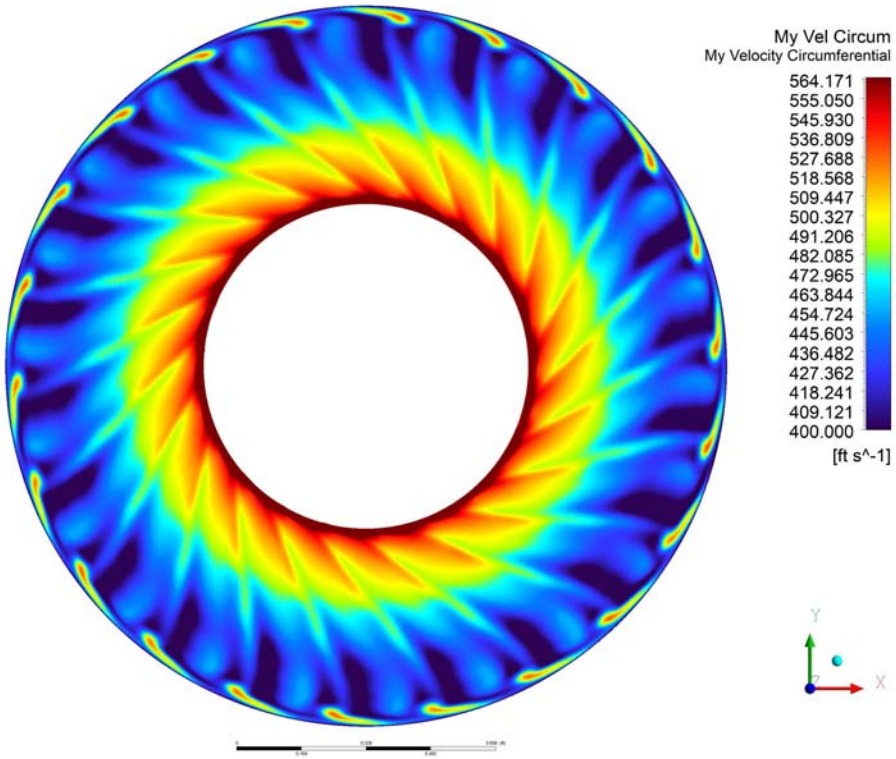

Figure 3.22: *Full-Annulus - Circumferential Velocity*

The entire Contour Plot of the velocities calculated in the Full-annulus analysis is reported for completeness (figure 3.21,3.22).

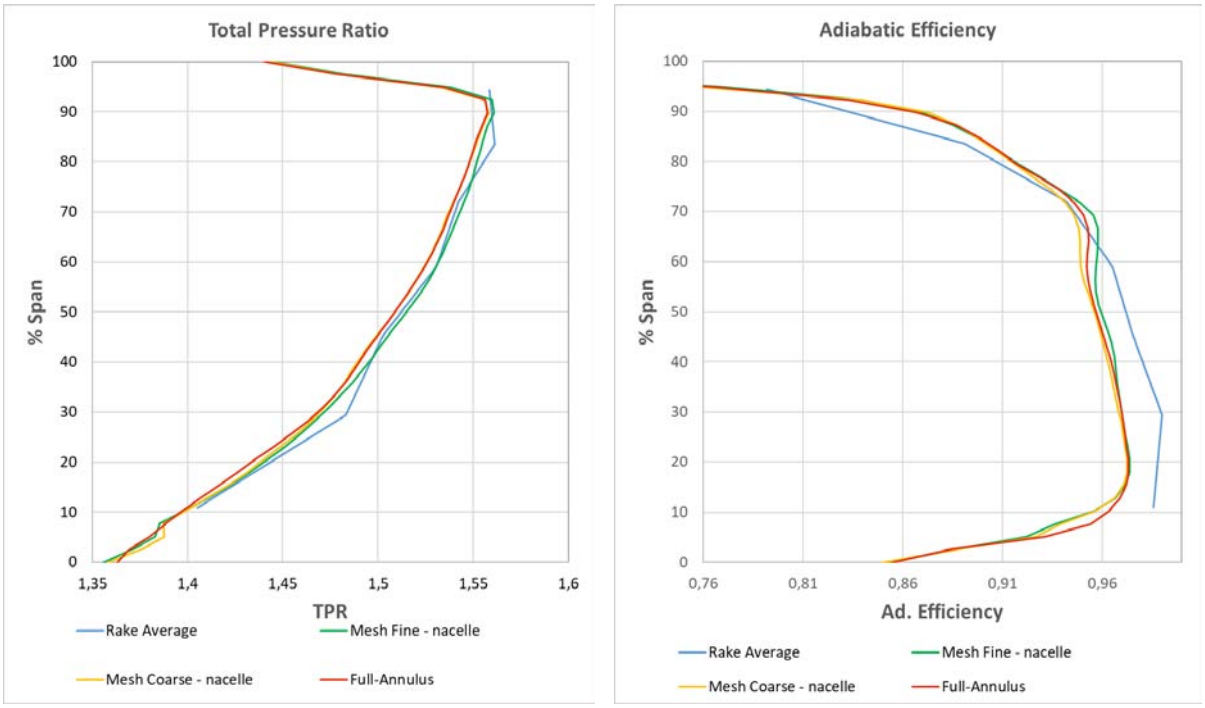

Figure 3.23: *Full-annulus Spanwise profile: TPR (Sx),Adiabatic Efficiency (Dx) - Take-off speedline.*

The Spanwise profiles show that the results do not differ much from those previously calculated, but are certainly better than the case of intubated fan where the effect of the Intake was not considered. Figure 3.28 shows what has just been described: the effect of Intake on the Fan inlet streamlines.

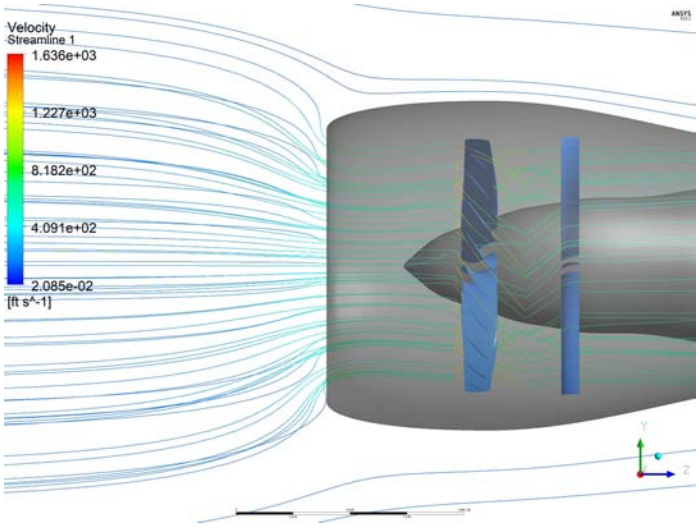

Figure 3.24: *Full-Annulus - Streamlines*

The last aspect to consider concerns the prediction of the Mach number along the blade. In the estimation of the relative Mach number there is a general improvement compared to previous cases. Unfortunately it was not possible to have an improvement in the wake estimation, in fact the problem of the mesh repetition zone remains. This could be related to the inability to improve the mesh at the periodic walls in Turbogrid. The only way would be to have a uniformly dense grid or meshing with another program and then import it into Cfx. In the Contour plot at 94% of the blade there is an improvement of the result obtained in single passage. Immediately after the L.E. there are no longer those areas at low speed difficult to explain until now. The only justification, however, having in general always decreased the number of mesh elements, must concern the approximation of the analysis in Single passage.

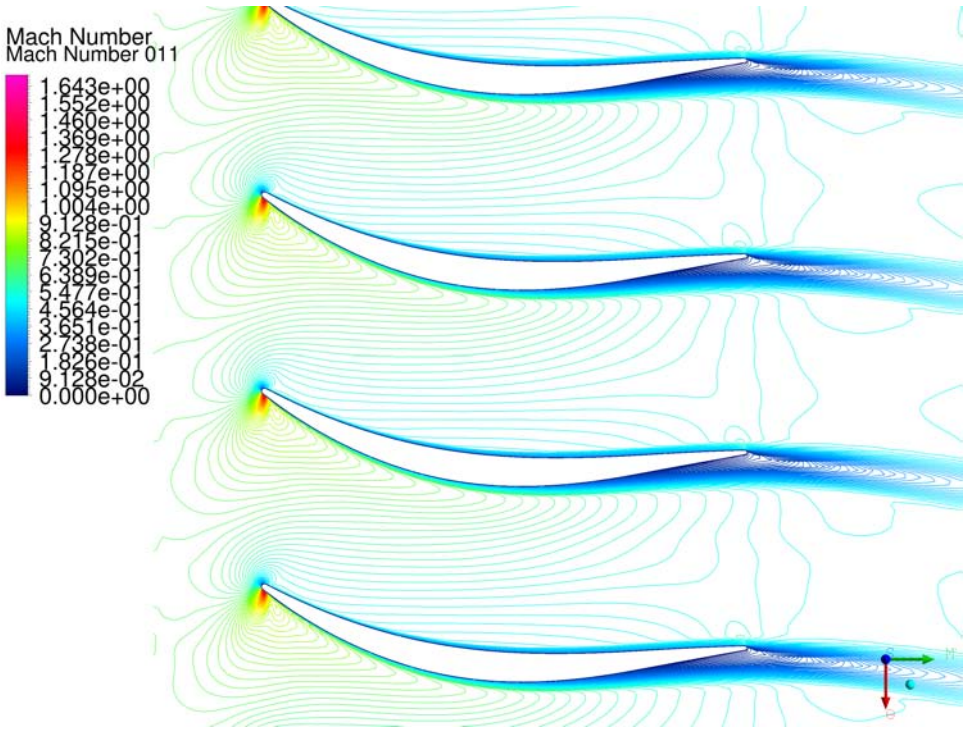

Figure 3.25: *Full-Annulus - Near Hub (11% span)*

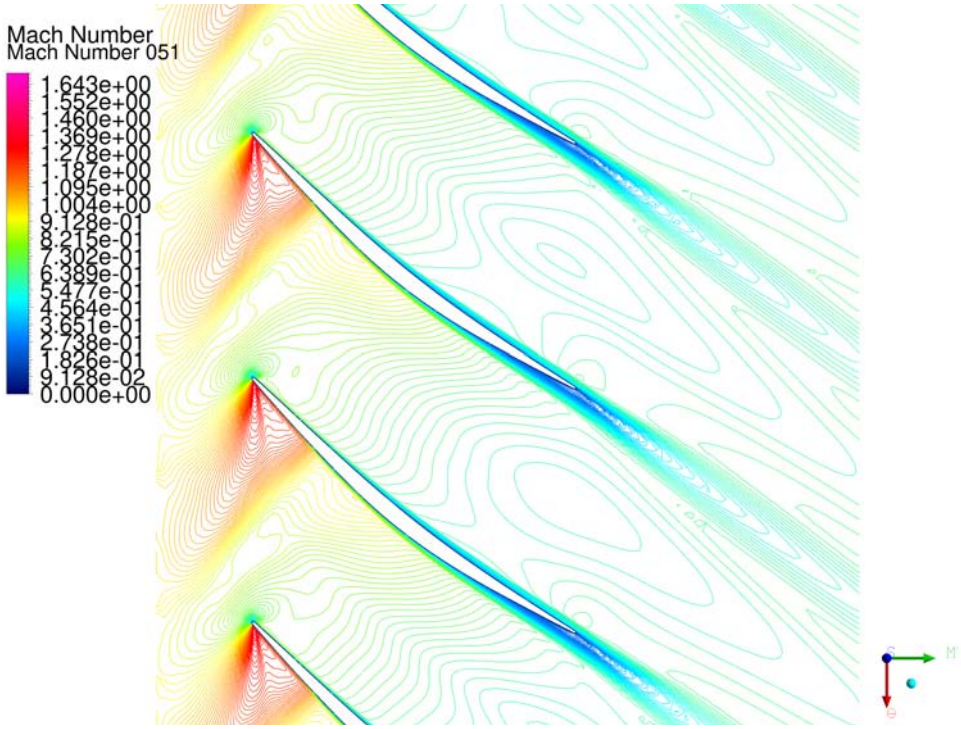

Figure 3.26: *Full-Annulus - Near mid (51% span)*

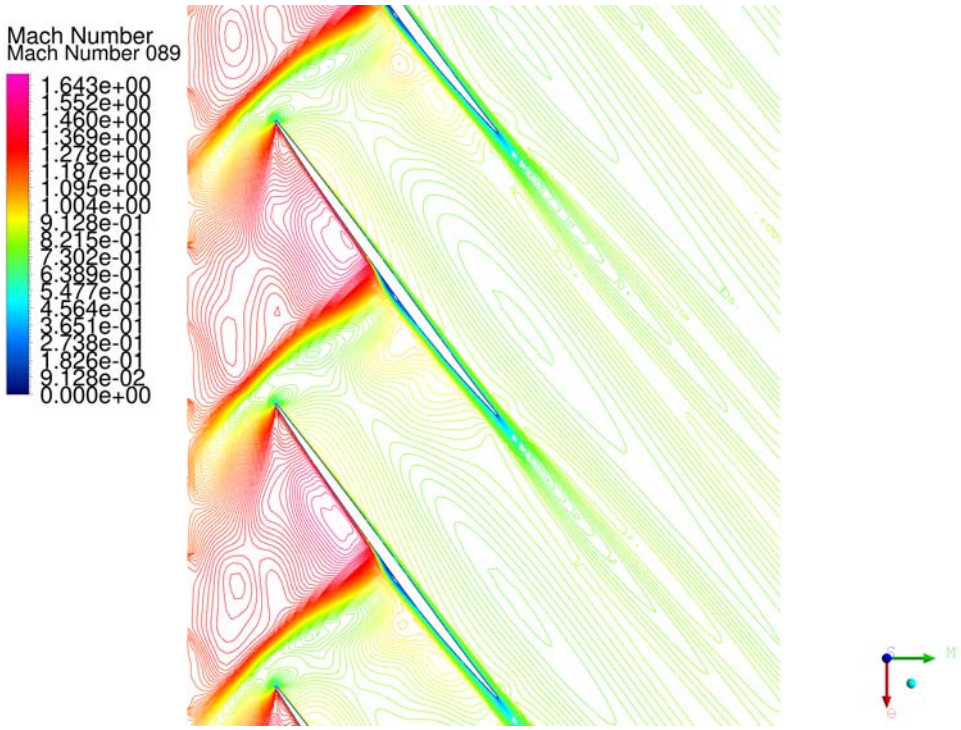

Figure 3.27: *Full-Annulus -Near tip (89% span)*

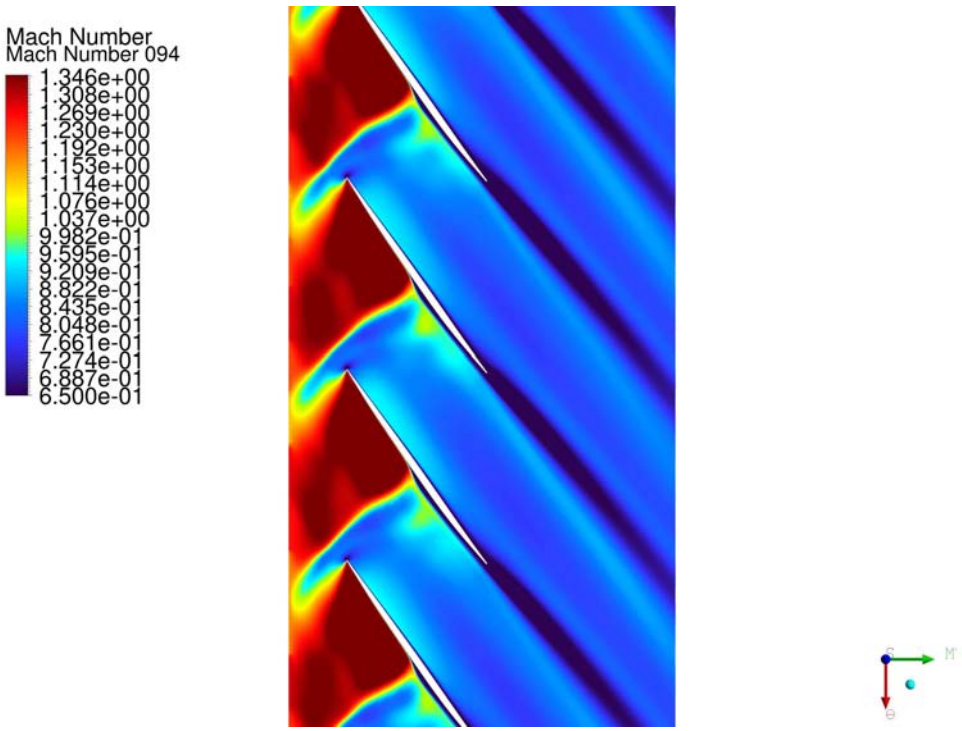

Figure 3.28: *Full-Annulus - Near tip (94% span)*

Conclusions

During the course of this thesis, it was possible to learn how to develop a CFD study from a relatively simple problem to its most complete version. The sensitivity study performed on the internal mesh of the channel allowed a considerable saving of elements and consequently CPU time. Considering the full-annulus analysis, the convergence of the solution was achieved with cycles of 250 iterations starting from the results of the single passage solution. The hardware used for the analysis was a Cluster consisting of 4 nodes with 32 GB of ram each, which took about 15 hours to complete a cycle of iterations. The mesh used for the rotor of the full-annulus model is constituted by 1/4 of the elements of the first Fine Mesh initially considered, so assuming that the Ram was sufficient, and would not have been, the time needed to complete 250 iterations would have been incredibly higher. Considering finally that the convergence of a solution is reached with several iteration cycles, it can be assumed that the main purpose of this thesis has been fully achieved.
The simulations performed have allowed to recreate with good approximation the experimental data of the test cases and CFD simulation carried out by NASA. The model created was analyzed with undisturbed flow conditions at the inlet, so although the flow respects the symmetry, the approach used passing through the model in Single passage was fundamental. It would have been very expensive at the computational level, with the tools available, a sensitivity study on the mesh of the complete system.
Finally this thesis can be used as a starting point for several subsequent studies such as the investigation of motion perturbations at the inlet of the fan or as a comparison for mathematical models that exemplify the rotor blade. Further studies could be carried out by analyzing the system under other operating conditions such as Overspeeding and Cruising by observing how the deformation of the stream lines and therefore of the flow at the inlet influences the internal fluid dynamics of the system. All these analyses can rely on a complete model consisting of a relatively small number of elements in relation to its complexity.

Appendix A

Mesh Extra Coarse

In this chapter are reported the contour plots obtained with the Extra coarse meshes, for Axial Velocity, Circumferential Velocity and relative Mach number.

A.1 Velocity component

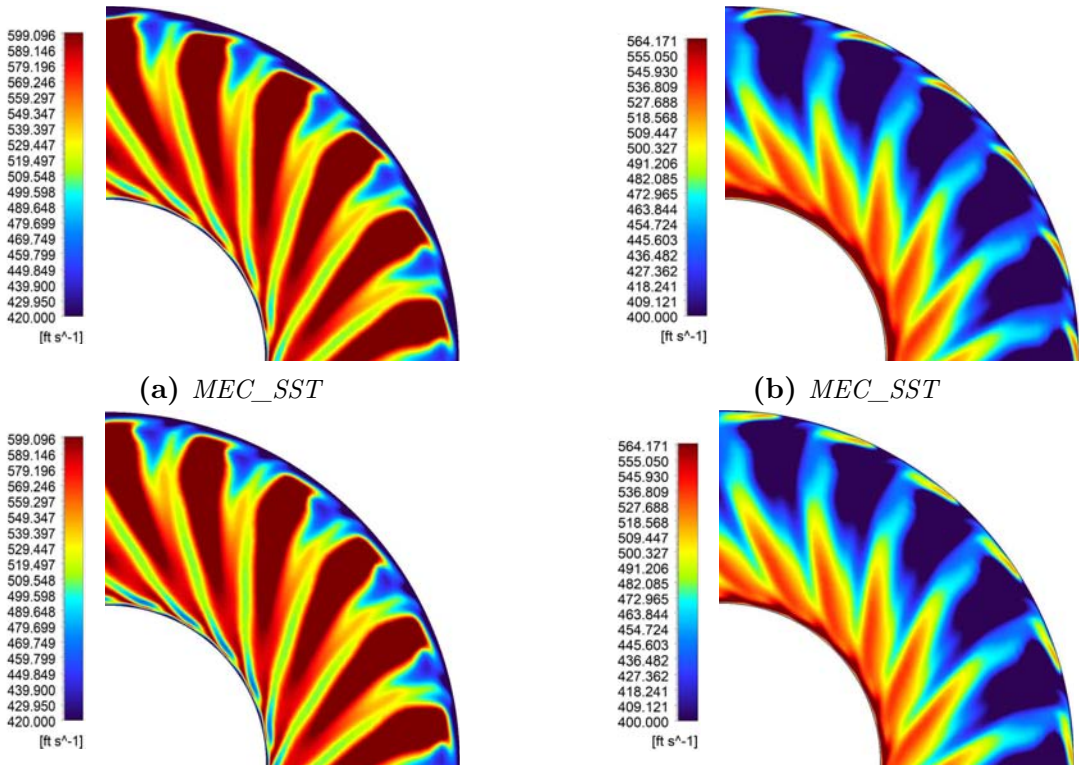

(a) *MEC_SST* **(b)** *MEC_SST*

(c) *MEC_RNG* **(d)** *MEC_RNG*

Figure A.1: *Contour plot of Axial Velocity (Sx) and Circumferential Velocity (Dx) - Take-off speedline - Inner Flow Channel*

Although the Extra Coarse Mesh with k-ε RNG turbulence model provided a better

prediction of the performance along the spanwise, from the contour plots some differences can be observed from the experimental measurement and from the simulations with the three Coarse, Medium and Fine meshes, for these reasons the turbulence model chosen and finally used in all the other simulations performed is the k-ω SST. In Figure A.1 (c) there are some low speed bubbles near the hub, this is certainly due to the different treatment of the boundary layer, even the Tip has a slight difference compared to previous cases, however, the low speed zones are not resolved correctly and the wake is still badly described. Figure A.1 (d) shows a propagation of the high-speed zones from the hub up to about 50% of the span, the differences with the experimental measurement in which the high-speed zone does not exceed 25% of the span are even more evident.

A.2 Relative Mach number

Between the two extra coarse Mesh there are some differences in correspondence of the Leading Edge and the Trailing Edge. In fact in the figure A.2 (a) is shown the SST turbulence model calculates Mach numbers higher at L.E. and a tighter wake compared to the RNG model. The position of the shock wave is the most significant information that can be obtained from the analysis of the plot near the blade tip. Depending on the turbulence model, the shock is estimated to occur at 39.5% of the chord by the SST model and 42% of the chord by the RNG model.

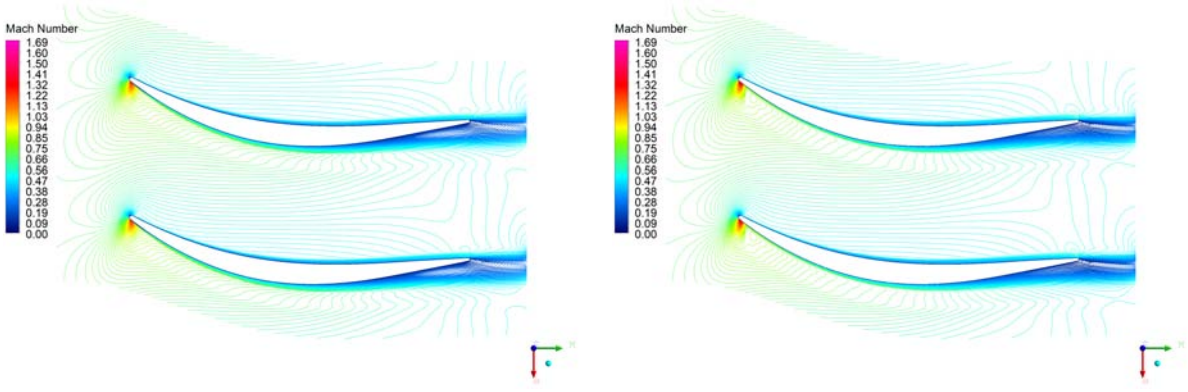

(a) *MEC_SST* **(b)** *MEC_RNG*

Figure A.2: *Near Hub Relative Mach number*

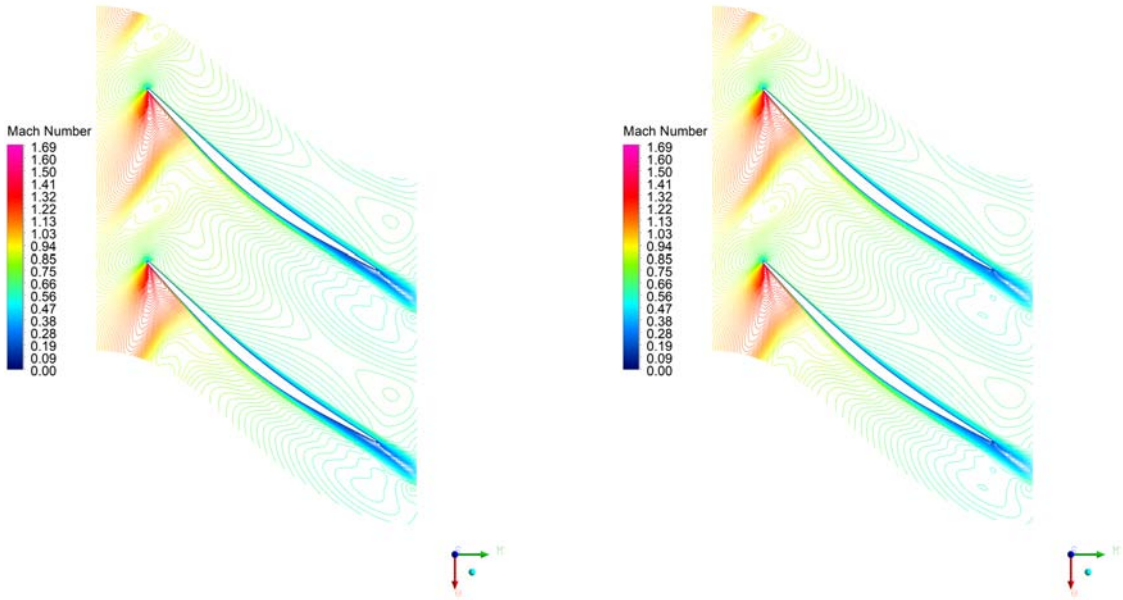

(a) *MEC_SST* **(b)** *MEC_RNG*

Figure A.3: *Near Mid Relative Mach number*

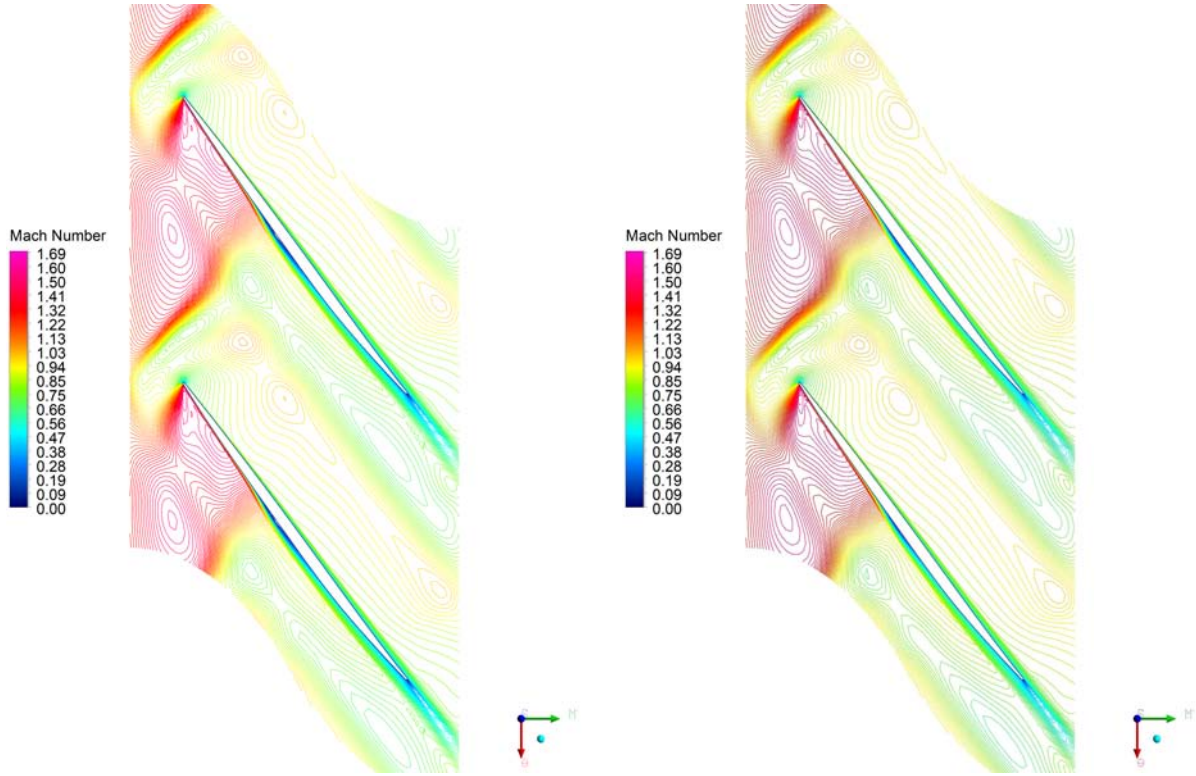

(a) *MEC_SST* **(b)** *MEC_RNG*

Figure A.4: *Near Tip Relative Mach number*

Appendix B

Mach Number near tip

This chapter compares the experimental measurement using LDV with the result of the various simulations with regard to the Mach number near the tip (94% of Span). These images provide conclusions similar to those obtained by comparing the contour plots of the NASA simulation, but being obtained at a higher span are reported as a further term of comparison between the model created and the experimental measurement. It is still evident that at the interface between the two blades the Mach number is badly described.

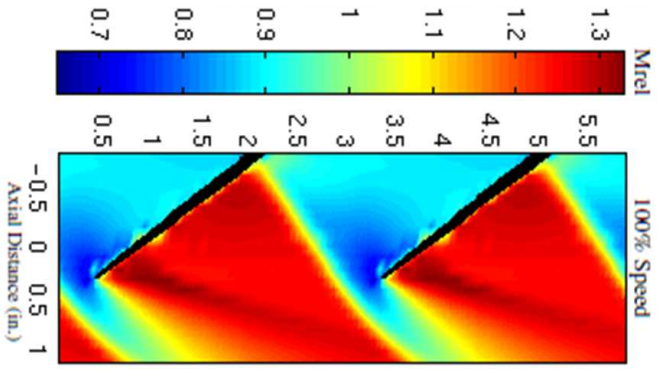

Figure B.1: *NASA Measurement [6]*

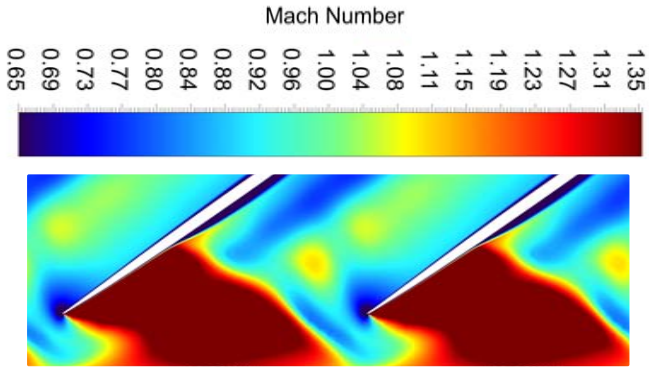

Figure B.2: *Mesh Coarse*

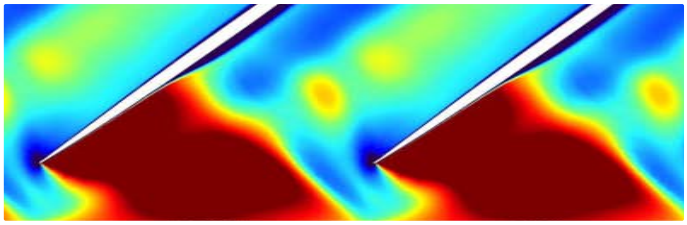

Figure B.3: *Mesh Medium*

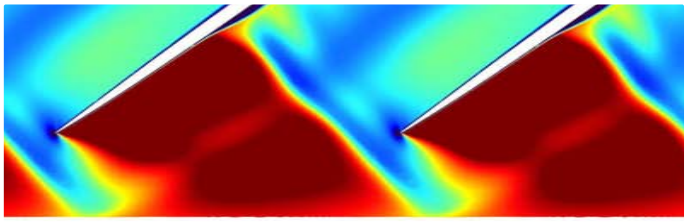

Figure B.4: *Mesh Fine*

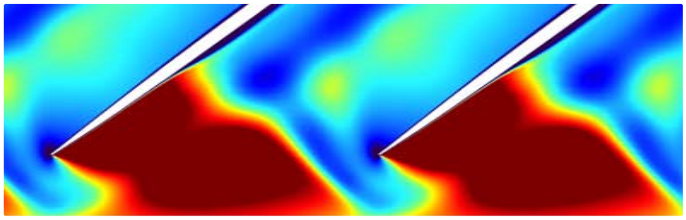

Figure B.5: *MEC SST*

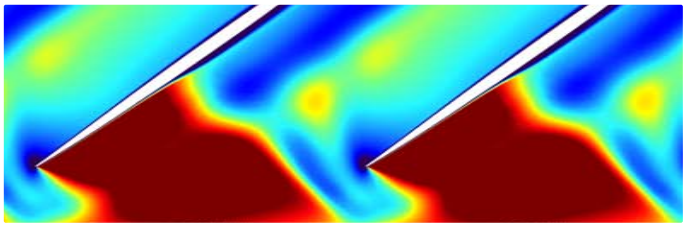

Figure B.6: *MEC RNG*

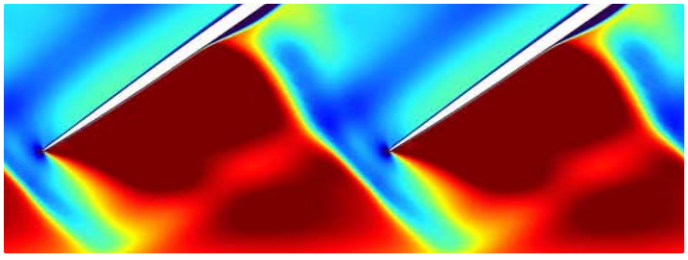

Figure B.7: *R4, M5, nacelle*

Bibliography

[1] C. Huges, R. Jeracki, R. Woodward and C. Miller. Fan Noise Source Diagnostic Test - Rotor Alone Aerodynamic Performance Results. *AIAA-2002-0374 or NASA/TM-2001-2111352.*

[2] D. Van Zante, G. Podboy, C. Miller and S. Throp. Testing and Performance Verification of a High Bypass Ratio Turbofan Rotor in an Internal Flow Component Test Facility. *NASA/TM-2009-215661.*

[3] Christopher E. Huges. Aerodynamic Performance of scale-model turbofan outlet guide vanes designed for low noise. *AIAA-2002-0374 or NASA/TM-2001-211352.*

[4] Daniel L. Tweedt. Computational Aerodynamic Simulation of a 1215 ft/sec Tip Speed Transonic Fan System Model for Acoustic Methods Assessment and Development. *NASA/CR-2001-218130.*

[5] Ismail B. Celik, U. Ghia, Patrick J. Roache, Christopher J. Freitas, H. Coleman, Peter E. Raad. Procedure for Estimation and Reporting of Uncertainty Due to Discretization in CFD Application. *Journal of Fluids Engineering JULY 2008, Vol.130/078001-1.*

[6] Gary G. Podboy, Martin J. Krupar, Christopher E. Huges and Richard P. Woodward. Fan Noise Source Diagnostic Test - LDV Measured Flow Field Results. *NASA/TM-2003-212330.*

[7] Gary G. Podboy, Martin J. Krupar, Christopher E. Huges and Richard P. Woodward. Steady and Unsteady Flow Field Measurements Within a NASA 22-inch Fan Model. *NASA/TM-2003-212329.*

[8] Ernesto Benini Propulsione Aerea. *Cleup 2005.*

[9] Philip G. Hill,Carl R. Peterson. Mechanics and Thermodynamics of propulsion. *Pearson 2010.*

[10] Saeed Farokhi Aircraft Propulsion. *Wiley 2014.*

Ringraziamenti

Non mi dilungherò più di tanto, ma qualche riga mi sembra doverosa.

In primis vorrei ringraziare il Prof. Benini per avermi dato l'opportunità di svolgere questa tesi e per tutte le conoscenze trasmesse. Vorrei ringraziare anche il mio correlatore Andrea Magrini poiché è stato sempre disponibile rispondendo a qualsiasi domanda e dubbio con precisione e competenza.

Questo risultato lo dedico ai miei genitori che in ogni momento di difficoltà hanno creduto in me e mi hanno supportato. Li ringrazio per tutto l'affetto dimostrato e per l'esempio che sono per me. Ringrazio mio fratello Davide perché mi ha sostenuto sempre e dato la carica con un sonoro "Alè!". Grazie alla Nonna Elena e a tutta la mia famiglia per aver condiviso i momenti di difficoltà e gioia di questo percorso.

Ringrazio Chiara perché in questo periodo mi è stata vicina più che mai.

Grazie a tutti gli amici per le avventure vissute in questi anni, vi porto nel cuore.

Grazie ai compagni di Università, per l'amicizia e l'ambiente stimolante che siamo riusciti a creare in questi anni.

Grazie davvero a tutti.